



**Universiteit Utrecht**



# Validating and quantifying the recovery efficiency increase of dedicated well configurations for aquifer storage and recovery (ASR) in brackish aquifers using a laboratory-scale sandbox model

---

**MSc research Earth Sciences (GEO4-1520)**

**Faculty of Geosciences**

**Utrecht University**

**Utrecht, the Netherlands**

**In cooperation with:**

**KWR: Watercycle Research Institute**

**Nieuwegein, the Netherlands**

**24 – 2 – 2017**

Author:	<b>Teun C.G.W. van Dooren</b>	<b>(3895327)</b>
Primary supervisor:	<b>prof. dr. Ruud J. Schotting</b>	<b>(Utrecht University)</b>
Secondary supervisor:	<b>dr. Niels Hartog</b>	<b>(Utrecht University &amp; KWR)</b>
Daily supervisor:	<b>dr. Koen G. Zuurbier</b>	<b>(KWR)</b>



## 0. Abstract

Aquifer storage and recovery (ASR) can be an important technique to help meet the increasing freshwater demand in coastal areas. It involves the infiltration and storage of freshwater in a suitable aquifer through a well during times when water is available and its recovery from the same well during times of need. Conventional ASR with a fully penetrating well (FPW-ASR) is generally unviable in brackish aquifers due to the buoyancy force on stored freshwater. However, field pilots suggest that dedicated multiple partially penetrating wells (MPPW-ASR) have the potential to increase the recovery efficiency ( $RE$ ) of ASR in brackish aquifers. The present study focused on validating and quantifying this improved recovery with use of a 2D lab-scale sandbox model, complemented by numerical SEAWAT simulations. A representative numerical 3D field-scale model with a normal fully penetrating well was able to validate the reduced  $RE$  of FPW-ASR with a lower dimensionless  $D$ -parameter, i.e. with a larger relative influence of buoyancy. The  $RE$  also reduced with a higher ratio of injection radius to aquifer height ( $r/H$ ), i.e. with a longer duration of infiltration. The latter observation contradicts previous studies, possibly due to numerical dispersion, and requires further research. Nevertheless, simulating ASR scenarios with different aquifer properties and operational parameters can result in the same  $RE$ , provided that  $D$ ,  $r/H$ , and the relative durations of the ASR phases are constant for a given grid discretization. This enabled downscaling of numerical ASR scenarios from field-settings to lab-settings. The improved  $RE$  of freshwater using MPPW-ASR instead of FPW-ASR in brackish aquifers was confirmed by the numerical 3D-field scale model. However, the  $RE$  of MPPW-ASR was not necessarily optimised because of the simplified operation in this study. When MPPW-ASR is optimised for a specific scenario, the  $RE$  can be further ameliorated. However, the potential relative improvement decreases with a less significant buoyancy effect (a lower  $r/H$  and a higher  $D$ ), because the  $RE$  of conventional ASR increases. The 2D sandbox was able to validate this performance. However, the results of a 3D-setting with a linear well were not transferrable to those of a 2D-setting with a planar well due to the difference in nature of both settings. Moreover, the experiments consistently underestimated the beneficial effect of MPPW-ASR that was observed in the numerical field-scale model with a vertical planar well. This probably resulted from the combined effect of measurement inaccuracies, heterogeneities in the aquifer packing, increased mixing due to the experimental well configuration, and (numerical) dispersion. The sandbox should thus be considered mainly as a validation and visualisation tool rather than a quantification tool.

## Keywords

Aquifer storage and recovery (ASR), brackish coastal aquifer, recovery efficiency ( $RE$ ), multiple partially penetrating wells (MPPW), laboratory-scale sandbox model



## Table of Contents

<b>0. Abstract.....</b>	<b>3</b>
<b>Keywords.....</b>	<b>3</b>
<b>Table of Contents.....</b>	<b>5</b>
<b>Nomenclature.....</b>	<b>7</b>
<b>Acknowledgements.....</b>	<b>7</b>
<b>1. Introduction .....</b>	<b>9</b>
<b>2. Methods.....</b>	<b>11</b>
2.1. <i>Representative field data .....</i>	11
2.2. <i>Experimental set-up: sandbox .....</i>	11
2.3. <i>SEAWAT .....</i>	13
2.4. <i>Numerical models .....</i>	14
2.5. <i>Metrics for scaling .....</i>	15
2.5.1. <i>Relative average displacement of the advective freshwater front (r/H).....</i>	16
2.5.2. <i>D-parameter of Bakker (2010).....</i>	17
2.6. <i>ASR scenarios.....</i>	17
2.7. <i>Metrics to quantify the results .....</i>	19
2.7.1. <i>Dimensions of the freshwater body.....</i>	19
2.7.2. <i>Vertical position of the centre of mass of freshwater (<math>z_{cm}</math>) .....</i>	19
2.7.3. <i>Mixing fraction (f(t)) .....</i>	20
2.7.4. <i>Recovery efficiency (RE).....</i>	20
<b>3. Results .....</b>	<b>21</b>
3.1. <i>Assessment of dispersivity.....</i>	21
3.2. <i>ASR performance in the representative numerical 3D-field setting .....</i>	22
3.3. <i>Comparison of the numerical 3D- and 2D-field model results.....</i>	23
3.3.1. <i>Slope of the fresh-salt interface (<math>\vartheta</math>) in the numerical 3D- and 2D-field models .....</i>	23
3.3.2. <i>Vertical position of the centre of mass (<math>z_{cm}</math>) in the numerical 3D- and 2D-field models .....</i>	24
3.3.3. <i>Recovery efficiency (RE) in the numerical 3D- and 2D-field models .....</i>	25
3.4. <i>Comparison of the numerical 2D-lab and 2D-filter model results.....</i>	27
3.4.1. <i>Infiltration behaviour of a vertical planar well and of individual filter screens.....</i>	27
3.4.2. <i>Slope of the fresh-salt interface (<math>\vartheta</math>) in the numerical 2D-lab and 2D-filter models.....</i>	28
3.4.3. <i>Recovery efficiency (RE) in the numerical 2D-lab and 2D-filter models .....</i>	29
3.5. <i>Comparison of the numerical 2D-filter model and the experimental results .....</i>	31
3.5.1. <i>Slope of the fresh-salt interface (<math>\vartheta</math>) in the numerical 2D-filter model and the experiments.....</i>	31
3.5.2. <i>Recovery efficiency (RE) in the numerical 2D-filter model and the experiments.....</i>	32
3.6. <i>Relative ASR performance of MPPW-ASR compared to FPW-ASR (%RE).....</i>	34

<b>4. Discussion .....</b>	<b>35</b>
4.1. Assessment of dispersivity .....	35
4.2. Influence of aquifer properties and operational parameters on the RE.....	35
4.2.1. Influence of aquifer properties and operational parameters on the RE of FPW-ASR.....	35
4.2.2. Influence of aquifer properties and operational parameters on the RE of MPPW-ASR .....	37
4.3. Scaling ASR from a numerical 3D-field setting to the experimental sandbox .....	37
4.3.1. Scaling ASR between the numerical 3D- and 2D-field settings.....	37
4.3.2. Downscaling ASR from a numerical 2D-field setting to a numerical 2D-lab setting .....	38
4.3.3. Discrepancies introduced by the well configuration.....	38
4.3.4. Discrepancies between the physical and numerical lab-scale models .....	39
4.4. Improved recovery efficiency (RE) of MPPW-ASR compared to FPW-ASR .....	40
4.4.1. Improved RE of MPPW-ASR compared to FPW-ASR in the representative field setting .....	40
4.4.2. Representativeness of the experimental sandbox.....	40
4.5. Implications for practical application .....	41
4.5.1. Additional controlling parameters for ASR in the field.....	41
4.5.2. Optimisation of MPPW-ASR .....	42
4.6. Recommendations .....	42
<b>5. Conclusions .....</b>	<b>45</b>
<b>6. References.....</b>	<b>47</b>
<b>7. Appendices.....</b>	<b>51</b>
7.1. Granulometric data of filtersand used in this research .....	51
7.2. Dimensions of the freshwater body and RE for all individual models and scenarios .....	52
7.3. Slope and position of the fresh-salt interface after infiltration (I) and storage (S) in all models for scenarios 4 – 9 .....	54
7.4. Vertical position of the centre of mass of freshwater ( $z_{cm}$ ) in the representative numerical 3D- and 2D-field settings.....	54
7.5. Mixing fraction versus the fraction of recovery for both FPW-ASR and MPPW-ASR in all models for scenarios 3 – 9.....	55
7.6. Infiltration pattern for scenario 2 in the experimental set-up.....	58
7.7. Evolution of the experimental freshwater body for scenario 4 .....	58
7.8. Freshwater body at the moment of salinization in the 3D-field model.....	59
7.9. Freshwater body at the moment of salinization in the 2D-field model.....	60

## Nomenclature

$C_{amb}$	=	salt concentration in the ambient groundwater [ $M L^{-3}$ ]
$C_{in}$	=	salt concentration in the infiltrated water [ $M L^{-3}$ ]
$C(t)$	=	salt concentration in the recovered water at time $t$ [ $M L^{-3}$ ]
$D$	=	dimensionless $D$ -parameter of Bakker (2010) (Eq. 8) [-]
$d_{50}$	=	median diameter of sand grains [L]
$f(t)$	=	mixing fraction as a function of time $t$ (Eq. 12) [-]
$H$	=	aquifer thickness [L]
$K$	=	hydraulic conductivity [ $LT^{-1}$ ]
$L$	=	length of the experimental sandbox [L]
$n$	=	porosity [-]
$Q$	=	pumping rate [ $L^3 T^{-1}$ ]
$Q_{2D}$	=	pumping rate of a vertical planar well in a 2D-setting (Eq. 3) [ $L^3 T^{-1}$ ]
$Q_{3D}$	=	pumping rate of a vertical linear well in a 3D-setting (Eq. 2) [ $L^3 T^{-1}$ ]
$RE$	=	recovery efficiency [-]
$r$	=	radial distance between the freshwater front and the well in a 3D-setting [L]
$r/H$	=	relative average displacement of the advective freshwater front (Eq. 6 & 7) [-]
$t$	=	time [T]
$v$	=	relative density difference between ambient water and infiltrated water [-]
$V$	=	volume of infiltrated water [ $L^3$ ]
$W$	=	width of the experimental sandbox [L]
$x$	=	linear distance between the freshwater front and the well in a 2D-setting [L]
$z_{cm, 2D}$	=	vertical position of the centre of freshwater mass in a 2D-setting (Eq. 11) [L]
$z_{cm, 3D}$	=	vertical position of the centre of freshwater mass in a 3D-setting (Eq. 10) [L]
$a$	=	dispersivity [L]
$\theta$	=	slope of the fresh-salt interface (Eq. 9) [-]
$\rho_f$	=	density of infiltrated freshwater [ $M L^{-3}$ ]
$\rho_s$	=	density of ambient brackish or saline groundwater [ $M L^{-3}$ ]
$\Delta h$	=	constant head difference used for infiltration in the experimental sandbox [L]
$\Delta RE$	=	absolute difference between the $RE$ of MPPW-ASR and FPW-ASR (Eq. 13) [-]
$\%RE$	=	relative difference between the $RE$ of MPPW-ASR and FPW-ASR (Eq. 14) [%]

## Acknowledgements

At first, I would like to thank dr. Niels Hartog and dr. Koen Zuurbier for their direct supervision during the whole research. I am especially grateful to both of them for sharing information obtained from the literature, for always being available for my questions, and for providing me with critical feedback. Moreover, I want to thank prof. dr. Ruud Schotting for being the supervisor of this research.

I wish to express sincere appreciation to Harry van Wegen and Sidney Meijering from the workplace of KWR for the construction of the experimental set-up. Additionally, I want to thank Wolter Siegers for his help during the lab-experiments. I also want to thank the Dutch company Filcom for providing the sand used in the experimental set-up.

Lastly, I want to thank the whole staff of the geohydrology group of KWR for being available for questions about numerical modelling or about the research in general.





## 1. Introduction

Coastal areas are the most densely populated regions in the world and have great economic importance (Small & Nicholls, 2003). However, the current increase of world's population and the associated freshwater demand are performing high stresses on freshwater resources in these zones. This results in societal as well as environmental problems (Vörösmarty et al., 2000). The sustainable development of these coastal areas may consequently be hampered and freshwater management will be put to the test.

A potential response to the freshwater stress is to store freshwater in times of surplus and to use it in times of need. This is especially valuable for regions with a strong seasonal precipitation regime (Merritt, 1986). Although solutions for freshwater problems are often sought at the Earth's surface, surface storage of freshwater may be inefficient due to space limitation, evaporation losses, anthropogenic contamination, and algal growth (Esmail & Kimbler, 1967). The subsurface may provide alternative and potentially more cost-efficient and sustainable solutions. Aquifer storage and recovery (ASR) involves the storage of water in a suitable aquifer through a well during times when water is available and its recovery from the same well during times of need (Pyne, 2005). It is increasingly being used to balance the seasonal supply and demand of freshwater (Maliva et al., 2006).

The recovery efficiency (*RE*), defined as the fraction of injected freshwater that can be recovered with a certain accepted quality, is an important performance indicator for ASR (Zuurbier et al., 2013; Van Ginkel et al., 2014). The *RE* depends on characteristics of the target aquifer, as well as on operational parameters. The former includes the aquifer thickness, hydraulic conductivity, isotropy, heterogeneity, and the density of the ambient groundwater. The latter includes the pumping rate, operational scheme, density of the injected water, and desired water quality during recovery. In general, a thin aquifer with a low hydraulic conductivity and strong anisotropy, a small density difference between both water bodies, and a large-scale ASR system with multiple-cycle operation, a short storage period and a high pumping rate would be beneficial for the *RE* of an ASR system (e.g. Esmail & Kimbler, 1967; Merritt, 1986; Missimer et al., 2002; Maliva et al., 2006; Ward et al., 2007; 2008; Zuurbier et al., 2013; Van Ginkel et al., 2014).

Conventional ASR operating with a fully penetrating well (FPW-ASR) can be unviable in coastal aquifers because of the density difference between infiltrated freshwater and ambient brackish or saline groundwater. The lighter freshwater tends to float upwards through the aquifer, while the denser ambient saline groundwater is recovered by lower parts of the well. As a result of this buoyancy effect, both water types are mixed upon extraction to form a generally unsuitable water quality (Esmail & Kimbler, 1967; Moulder, 1970; Merritt, 1986; Ward et al., 2007; Zuurbier et al., 2013).

Field pilots suggest that the *RE* of an ASR system in coastal aquifers can be increased by implementing dedicated well configurations, such as multiple partially penetrating wells (MPPW-ASR) or horizontal directional drilled wells (HDDW-ASR) (Zuurbier et al., 2014; 2015). These configurations are primarily based on an increased vertical control on freshwater injection and recovery, optionally complemented by interception of deeper saline or brackish groundwater and thus by counteracting the buoyancy effect. However, mixing with ambient saline groundwater will remain a source of freshwater loss and the system will never attain an *RE* of 100%, unless reverse osmosis is also implemented to post-treat recovered water (Zuurbier et al., 2014; 2016b).

Although field pilots and computer models have already demonstrated the potential of dedicated well configurations for ASR in brackish aquifers (Zuurbier et al., 2014; 2015), physical models remain important visualisation tools to gain and provide information about the interaction between fresh and saline water and the effects of groundwater extraction (Stoeckl & Houben, 2012). Several objectives can be pursued with a physical model

(Svendsen, 1985). Pennink (1915), Werner et al. (2009) and Zhao et al. (2009) performed lab experiments on lens generation and upconing of ambient saline groundwater due to freshwater extraction. Moreover, Van Ginkel et al. (2016) studied the effect of flow barriers on ASR in a saline aquifer. These studies all pursued the aim to provide quantitative insights into a phenomenon not yet described in theory or understood in practice. Goswami & Clement (2007), Luyun et al. (2011), and Robinson et al. (2016) studied the dynamics of saltwater intrusion in coastal aquifers and Stoeckl & Houben (2012) determined flow patterns and travel times resulting from freshwater infiltration and extraction in a saline aquifer. These studies were done to obtain measurements for phenomena that are too complicated to be accessible for theoretical approaches.

To date, physical models have not been used for the understanding of dedicated well configurations for ASR systems in coastal aquifers. Therefore, the objective of this study was to explore to what extent an experimental sandbox model can validate the general benefits of MPPW-ASR, as Zuurbier et al. (2014) described for a field setting, and how the results of a physical sandbox model compare to those of numerical model simulations. The main hypothesis is stated as:

- *The recovery efficiency increase that can be expected when MPPW-ASR is used instead of FPW-ASR in brackish aquifers can be validated and quantified with a physical sandbox model.*

The following research questions were studied to test this hypothesis:

- *How do the aquifer properties and operational parameters influence the RE of FPW-ASR and MPPW-ASR, and which of these controlling parameters are scalable to what extent?*
- *How can a representative field setting of both conventional ASR and MPPW-ASR effectively be downscaled to the experimental sandbox, and how can the introduced discrepancies be explained?*
- *What is the improvement in the RE of MPPW-ASR compared to FPW-ASR for different situations in a representative field setting and in the experimental sandbox?*
- *What are the implications of the results for the practical application?*

## 2. Methods

### 2.1. *Representative field data*

Field data for actual ASR systems were used as representative data for the experiments and numerical simulations. A confined brackish aquifer in the Westland area of the Netherlands was chosen for this purpose, in which ASR systems are currently operating to inject and store the winter precipitation surplus for later recovery of freshwater during the growing season for greenhouse horticulture. The characterization of the subsurface in the Westland area is well documented by Zuurbier et al. (2013; 2014), Zuurbier & Paalman (2014), Ros & Zuurbier (2016), and Zuurbier & Stuyfzand (2016). In *Table 1*, the most important information from these studies is summarized for the target aquifer for ASR systems.

**Table 1:** Properties of the target aquifer in the Westland area that have been documented by Zuurbier et al. (2013; 2014), Zuurbier & Paalman (2014), Ros & Zuurbier (2016) and Zuurbier & Stuyfzand (2016).

<b>Parameter</b>	<b>Value</b>
Top elevation [m-BSL]*	13 – 22
Bottom elevation [m-BSL]*	37 – 41
Thickness [m]	15 – 28
Horizontal hydraulic conductivity [ $m d^{-1}$ ]	35 – 100
Vertical Hydraulic conductivity [ $m d^{-1}$ ]	35 – 100
Effective porosity [-]	0.3
Specific storage [-]	$10^{-7}$
TDS concentration [ $mg L^{-1}$ ] **	8682
Diffusion coefficient [ $m^2 d^{-1}$ ]	$8.64 \cdot 10^{-5}$

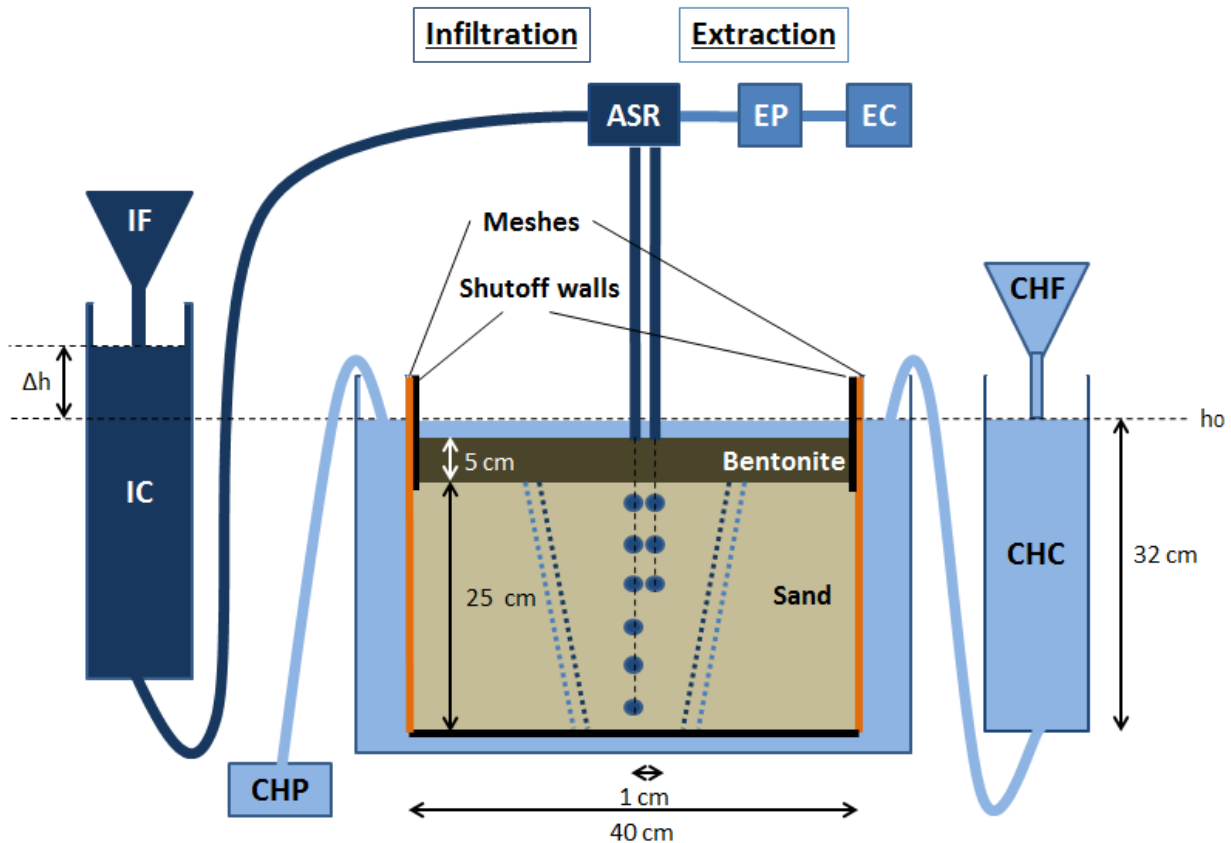
\*m-BSL is the abbreviation for meters below sea level.

\*\*TDS is the abbreviation for total dissolved solids.

### 2.2. *Experimental set-up: sandbox*

The sandbox used in this research (*Figure 1*) was made of a stainless steel frame with glass walls, which enabled cross-sectional visualisation of density-dependent flow patterns. The left and right boundaries were bounded by saltwater reservoirs that functioned as constant head boundaries, which were separated from the main section by perforated plates and fine mesh screens (Goswami & Clement, 2007; Luyun et al., 2011). They were interconnected below the main section. The internal dimensions of the sandbox were 40 x 36 x 10 cm (L x H x W), excluding the interconnected constant head reservoirs, which were 5 cm wide.

The sand used in this study was filtersand obtained from the Dutch company Filcom and had a grain size ranging from 200 to 630  $\mu m$  with a median grain size ( $d_{50}$ ) of 388  $\mu m$  (*Appendix 7.1*). This compared well to the median grain size of 400  $\mu m$  for sand found in the target aquifer in the Westland area of the Netherlands (*Table 1*). The ambient saline water was prepared by dissolving table salt at the required concentration (17.4  $g L^{-1}$  TDS) in deionized water. After filling the sandbox with this saltwater, a construction of several filter screens that covers approximately the whole width (10 cm) of the sandbox was placed in the middle of it to function as an ASR-well (*Figure 2*). The sand was saturated with water of the same salinity and subsequently poured into the main section of the sandbox. The sand was simultaneously compacted under fully saturated conditions by the tamping compaction method of Rietdijk et al. (2010) until the sand reached a height of 25 cm. This method has been proven to be the most suitable, representative, and reproducible method to generate uniform fully saturated porous media with a high relative density and to eliminate redistribution of sand (Van Dooren, 2015). After applying the tamping compaction method of Rietdijk et al. (2010), the sand had a saturated hydraulic conductivity ( $K$ ) of 55  $m d^{-1}$  and a porosity ( $n$ ) of 0.33 (Van Dooren, 2015), which were both representative for the Westland area (*Table 1*). The height of 25 cm allowed to install 6 filter screens into the aquifer.



**Figure 1:** The experimental set-up that was used in this research consists of the following compartments: IF: Volumetric flask for infiltration, IC: Infiltration cylinder, ASR: ASR-well, EP: Extraction pump, EC: EC-meter (Tetracon 325 conductivity cell) in a glass 50 mL cup, CHF: Volumetric flask for constant heads, CHC: Constant head cylinder, and CHP: Constant head pump. The meshes and the shutoff walls are indicated as well. The dark blue colour represents the fresh infiltration water and the light blue colour represents the ambient saline water. The blue dots represent the individual filter screens of the ASR-well inside the aquifer (Figure 2). The blue dotted lines in the aquifer represent a potential density-dependent infiltration pattern.

A 5 cm thick layer of bentonite clay was deposited on top of the sand after the meshes were closed by shutoff walls just below the top of the aquifer to prevent them from transporting bentonite. The bentonite had a low hydraulic conductivity of  $9 \cdot 10^{-6} \text{ m d}^{-1}$  (Marton Geotechnical Services Ltd., 2015) and thus served as a confining layer on top of the aquifer. Bentonite was preferred over an impermeable layer with a smooth interface, as preferential flow pathways would likely be introduced at the top of the aquifer.

The physical model was flanked by another cylinder, containing deionized water ( $0 \text{ g L}^{-1}$  TDS) for infiltration (Figure 1: IC). The tracer dye 'Brilliant Blue FCF' (Waldeck GmbH & Co. KG, Germany) was dissolved in it at a concentration of  $0.2 \text{ g L}^{-1}$  for visualisation. The effect of the tracer on density and viscosity was assumed to be negligible.

The level of saltwater in the constant head boundary reservoirs was kept constant at 32 cm by a peristaltic pump during infiltration (Figure 1: CHP) and by turning a glass volumetric flask upside down at the same elevation in a connected constant head cylinder during extraction (Figure 1: CHC; CHF). Infiltration rates were controlled by using a constant head difference (Figure 1:  $\Delta h$ ) between the water level in the sand tank and the applied head in the infiltration cylinder. For this purpose, a glass volumetric flask was turned upside down at the correct height in the infiltration cylinder (Figure 1: IF). This infiltration method prevented the infiltration of air. The infiltration rates were indirectly measured by measuring the volume of saltwater extracted by the constant head pump over time (Figure 1: CHP). Extraction rates were controlled by a peristaltic pump and were directly measured by determining the extracted volume over time (Figure 1: EP).

Infiltration was performed with the well that has six filter screens on each side, distributed over the complete aquifer thickness. Extraction in FPW-ASR was performed with the same well, whereas extraction in MPPW-ASR was performed with the well that has three filter screens in the upper half of the aquifer (Figure 1 and 2). The filter screens can not operate individually in this set-up. The construction was rather assumed to approximate a single fully penetrating vertical planar well for infiltration, and a single partially penetrating planar well over only the upper half of the aquifer for extraction in MPPW-ASR. As a result, the well configuration and operation were not optimised for MPPW-ASR to obtain the highest RE possible, just as Zuurbier et al. (2014) did by selecting the most suitable part of the aquifer for injection and recovery at a certain time. The experimental well-configuration and ASR operation were rather simplified because of the limitations of the set-up and because it allowed to keep the construction in the sandbox in between several experiments. Although it does actually not consist of multiple partially penetrating wells, the term MPPW-ASR will still be used throughout this report for the implemented well-configuration.

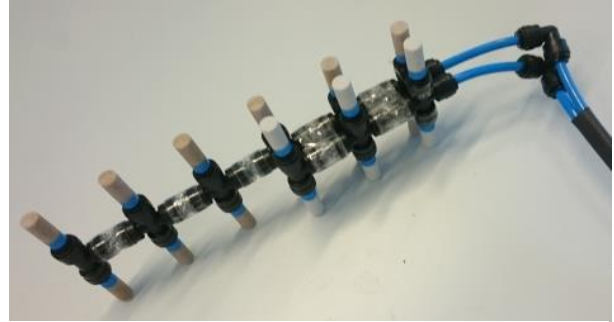


Figure 2: Configuration of the ASR-well used in the experimental set-up (Figure 1). The left well consists of six horizontal filter screens and was placed in the centre of the aquifer. The right well consists of three horizontal filter screens. All screens had a thickness of 1 cm, a width of 9.7 cm, and a vertical spacing of 4 cm.

### 2.3. SEAWAT

SEAWAT Version 4 (Langevin et al., 2008) was used via PMWIN version 8 (Chiang, 2012) to construct numerical models for the simulation of ASR systems in coastal aquifers. SEAWAT is a finite difference model that is able to simulate three-dimensional, variable-density, transient, saturated groundwater flow in porous media. It solves the coupled groundwater flow and solute transport equations of MODFLOW and MT3DMS in terms of fluid density and equivalent freshwater heads. For more sophisticated information about the calculation procedure of SEAWAT, the reader is referred to Guo & Langevin (2002) and Langevin et al. (2008).

Water densities ( $\rho$ ) [ $\text{kg m}^{-3}$ ] were calculated in SEAWAT with the TDS concentration [ $\text{g L}^{-1}$ ] and the following linear relationship, in which  $1000 \text{ kg m}^{-3}$  was used as the reference density of freshwater (Zuurbier et al., 2014):

$$\rho(TDS) = 0.7 TDS + 1000 \quad \text{Eq. 1}$$

The flow and transport equations were solved with the data in Table 2. In addition, the third-order total-variation-diminishing (ULTIMATE) scheme was used with a Courant number of 0.75 to solve for advective transport. This combination resulted in a mass conservative calculation and prevented the occurrence of excessive numerical dispersion and negative concentrations resulting from spurious oscillations (Zheng & Wang, 1999; Zheng & Bennett, 2002; Herrera & Valocchi, 2006; Chiang, 2012; Schäfer, 2016).

Table 2: Properties and parameters used in SEAWAT to solve the coupled groundwater flow and solute transport equations.

	Groundwater flow	Solute transport
<b>Model</b>	MODFLOW	MT3DMS
<b>Solver</b>	Preconditioned conjugate gradient package 2 (PCG2)	Generalized conjugate gradient (GCG)
<b>Preconditioning method</b>	Modified Incomplete Cholesky	Jacobi
<b>Maximum number of outer iterations</b>	50	50
<b>Maximum number of inner iterations</b>	100	250
<b>Concentration closure criterion</b>	-	$10^{-11}$

## 2.4. Numerical models

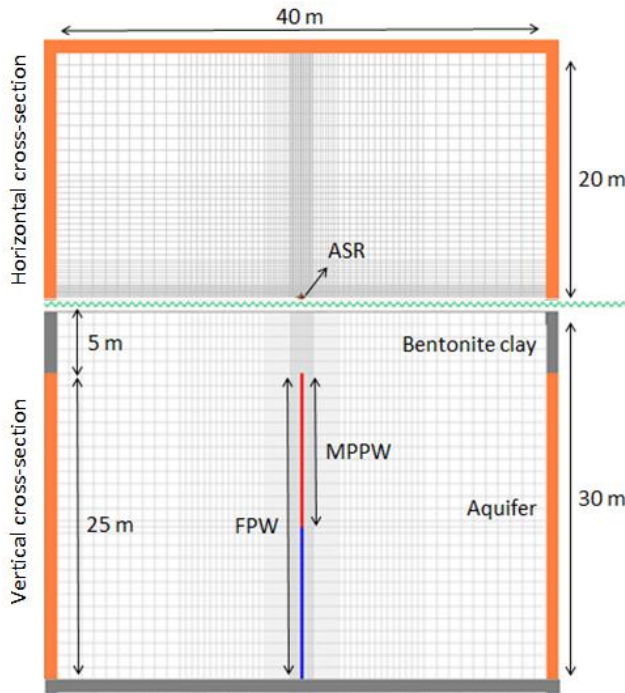
Several numerical models were constructed in SEAWAT and were used to downscale a representative field scale model to the lab-experiments (*Figure 3*).

<b>A</b>	<ul style="list-style-type: none"> <li>• Dimension: 3D</li> <li>• Setting/scale: Field</li> </ul>	<ul style="list-style-type: none"> <li>Method: Numerical</li> <li>Well type: vertical &amp; linear</li> </ul>
<b>B</b>	<ul style="list-style-type: none"> <li>• Dimension: 2D</li> <li>• Setting/scale: Field</li> </ul>	<ul style="list-style-type: none"> <li>Method: Numerical</li> <li>Well type: vertical &amp; planar</li> </ul>
<b>C</b>	<ul style="list-style-type: none"> <li>• Dimension: 2D</li> <li>• Setting/scale: Lab</li> </ul>	<ul style="list-style-type: none"> <li>Method: Numerical</li> <li>Well type: vertical &amp; planar</li> </ul>
<b>D</b>	<ul style="list-style-type: none"> <li>• Dimension: 2D</li> <li>• Setting/scale: Lab</li> </ul>	<ul style="list-style-type: none"> <li>Method: Numerical</li> <li>Well type: individual filter screens</li> </ul>
<b>E</b>	<ul style="list-style-type: none"> <li>• Dimension: 2D</li> <li>• Setting/scale: Lab</li> </ul>	<ul style="list-style-type: none"> <li>Method: Experimental</li> <li>Well type: individual filter screens</li> </ul>

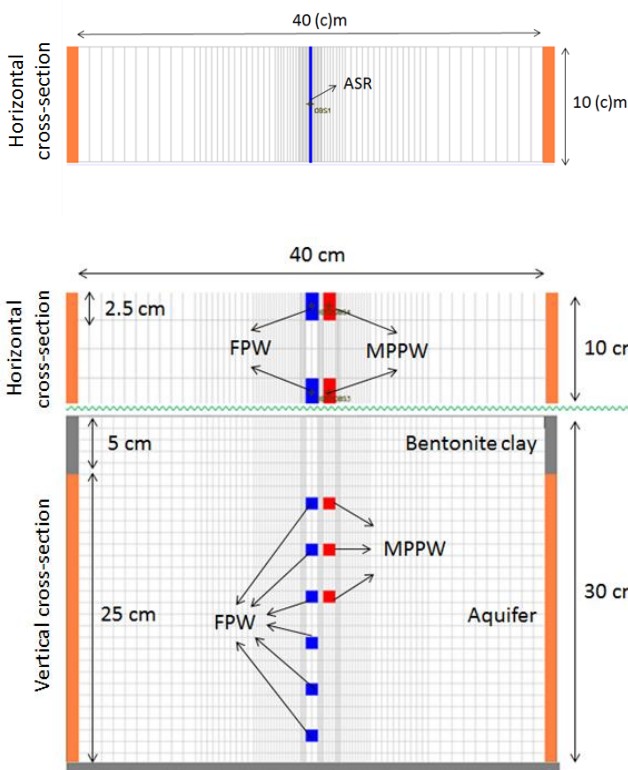
**Figure 3:** The five models used in this study. The experimental lab-scale model (model E) was already described in Section 2.2. The four remaining numerical models (models A-D) are described in this section and the metrics and procedure for scaling between all models is described in Section 2.5.

The general properties of the representative target aquifer in the Westland area (*Table 1*) were implemented for all numerical models, with a  $K$  of 55 m d<sup>-1</sup> and a  $n$  of 0.33 that correspond with the sand used in the experimental set-up (Van Dooren, 2015). In addition, a realistic value for the specific yield of medium grained sand was 0.25 (Fitts, 2002). For the lab-scale models, a 5-cm thick confining bentonite clay layer with a conductivity of 9\*10<sup>-6</sup> m d<sup>-1</sup> was modelled on top of the aquifer, just as in the experimental set-up. The initial hydraulic head was 32 cm for the complete domain, i.e. 2 cm above the top of the bentonite clay. The dimensions of the field-scale models were 100 times larger compared to those of the lab-scale models. The domains of the four different numerical models are presented in *Figure 4 - 6*, with more specific information given in the captions. Infiltration was performed over the complete aquifer thickness in all models, whereas only the upper half of the aquifer was used for extraction in MPPW-ASR.

The 3D-field model (model A; *Figure 3 and 4*) was simulated as a representative field application of ASR to determine implications for the practical application. The 2D-field model (model B; *Figure 3 and 5*) was simulated to determine the scalability and discrepancies between 3D- and 2D-settings. The results of the 2D-field model were compared to those of the 2D-lab model (model C; *Figure 3 and 5*) to determine the potential of downscaling ASR systems. Lastly, the 2D-filter model (model D; *Figure 3 and 6*) was simulated to determine the offset introduced by the implemented well-configuration, to guide the laboratory experiments and predict the results (model E; *Figure 1 and 3*), and to discuss the discrepancies between numerical and physical modelling.



**Figure 4:** Horizontal cross-section through the aquifer (top) and vertical cross-section through the well (bottom) of the **numerical 3D-field scale model** (model A; Figure 3). Taking advantage of the radial symmetry of an ASR system, a vertical linear well of 0.1 m in radius ('ASR') was placed in the middle at the front boundary of a half-domain area of 8 ha and all pumping rates were reduced to 50% of the actual values, thereby reducing the computation time (Maliva et al., 2006; Ros & Zuurbier, 2016). As MPPW-ASR wells are often installed in the same borehole as FPW-ASR wells, both wells were located in the middle of the domain. Cells of 0.1 x 0.1 m were applied within a radius of 1 m from the well. The cell size subsequently increases to 0.25 x 0.25 m, 0.5 x 0.5 m, and 1 x 1 m within a radius of 3, 10, and 20 meters from the well. Both the aquifer and the bentonite clay were divided in 1 m-thick layers (and 0.5 m for layers 18 & 19). The IBOUND and ICBUND values for the external lateral model boundaries in the bentonite clay were 0 to generate no-flow boundaries (gray) and those in the target aquifer were -1 to generate constant head boundaries with a constant salt concentration (orange). The base of the domain was also modelled as a completely impermeable layer (gray).



**Figure 5:** Horizontal cross-section through the aquifer of the **numerical 2D-models with a vertical planar well** (models B and C; Figure 3). A cross-section was taken through the ASR-well in the 3D-field model (Figure 4) and was given a width of 10 m to construct the 2D-field model (model B; Figure 3). The vertical cross-sectional properties are therefore equal to those of the 3D-field model. The same model was initially also constructed for the numerical lab-scale model (model C; Figure 3) but all spatial parameters were converted to cm to create a model that corresponded with the dimensions of the experimental model.

**Figure 6:** Horizontal cross-section through the aquifer (top) and vertical cross-section through the well (bottom) in the **numerical 2D lab-scale model with the individual filter screens** (model D; Figure 3). The horizontal cross-section was divided in 4 rows of 2.5 cm and the six individual filters of 1 cm in diameter were included in rows 1 and 4. They were equally spaced between elevations of 2 and 23 cm for FPW. The three MPPW-screens were located 0.1 cm to the right of the middle due to technical issues, thereby introducing a discrepancy compared to the 2D-lab model (model C; Figure 3). The total pumping rate was equally distributed over all individual filter

## 2.5. Metrics for scaling

Direct scaling between 3D- and 2D-settings is generally impossible, since a vertical linear well results in axi-symmetric flow patterns, whereas a vertical planar well in 2D flow patterns. Nevertheless, scaling between the numerical 3D-field model and the numerical 2D-field model was attempted by equalizing two dimensionless parameters for a given ASR scenario. The same strategy was used for downscaling the 2D-field model to the 2D-lab model, and for scaling between the individual lab-scale models and the experiments.

### 2.5.1. Relative average displacement of the advective freshwater front ( $r/H$ )

The first dimensionless parameter that was equalized in all models (Figure 3) was the relative average displacement of the advective freshwater front after infiltration ( $r/H$ ). The definition of the pumping rate ( $Q$ ) [ $L^3 T^{-1}$ ] (Figure 7) was used to determine this parameter. Any effects of density, diffusion and dispersion were disregarded at this stage.

The pumping rate in a 3D-setting with a vertical linear well ( $Q_{3D}$ ) (Figure 7) is defined as:

$$Q_{3D} = \frac{dV}{dt} = \frac{d(nH\pi r^2)}{dt} = nH\pi \frac{dr^2}{dt} \quad \text{Eq. 2}$$

And the pumping rate in a 2D-setting with a vertical planar well ( $Q_{2D}$ ) (Figure 7) as:

$$Q_{2D} = \frac{dV}{dt} = \frac{d(2nHWx)}{dt} = 2nHW \frac{dx}{dt} \quad \text{Eq. 3}$$

In these equations,  $H$  and  $W$  refer to the height and the width of the aquifer, respectively [ $L$ ].  $x$  and  $r$  are the linear and radial distances between the freshwater front and the well, respectively [ $L$ ], and  $n$  is the porosity [-]. Furthermore,  $V$  represents the volume of freshwater that is infiltrated [ $L^3$ ] and  $t$  is the duration of infiltration [ $T$ ].

For constant pumping rates ( $dQ/dt = 0$ ), Eq. 4 and 5 are obtained:

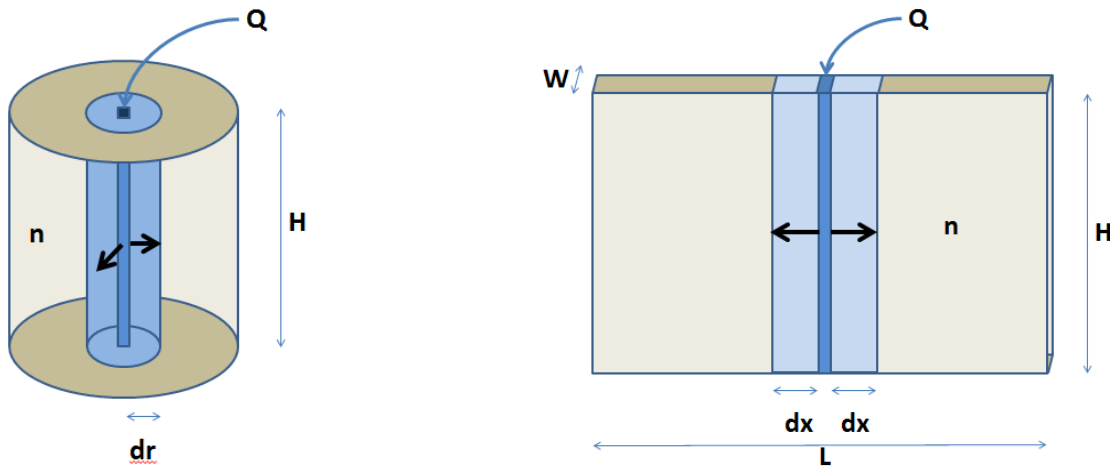
$$r(t) = \sqrt{\frac{Q_{3D}t}{nH\pi}} \quad \text{Eq. 4}$$

$$x(t) = \frac{Q_{2D}t}{2nHW} \quad \text{Eq. 5}$$

The relative average displacement of the freshwater front compared to the height of the aquifer is defined as Eq. 6 for a 3D-setting and as Eq. 7 for a 2D-setting, respectively.  $r/H$  is the dimensionless parameter that represents either Eq. 6 or 7 after infiltration, depending on the setting, and which was equalized in every model.

$$\frac{r(t)}{H} = \sqrt{\frac{Q_{3D}t}{n\pi H^3}} \quad \text{Eq. 6}$$

$$\frac{x(t)}{H} = \frac{Q_{2D}t}{2nWH^2} \quad \text{Eq. 7}$$



**Figure 7:** Freshwater motion resulting from pumping in an aquifer for a 3D- setting with a linear fully penetrating well (left) and for a 2D-setting with a planar fully penetrating well (right).  $H$ ,  $W$  and  $L$  refer to the height, width and length of the aquifer, respectively [ $L$ ].  $x$  and  $r$  are the linear and radial flow directions, respectively [ $L$ ], and  $n$  is the porosity [-]. The dark blue colours indicate the position of the well and the light blue colours the position of the freshwater body. The flow directions within the aquifer are indicated with black arrows.



### 2.5.2. *D*-parameter of Bakker (2010)

As the interface between the infiltrated freshwater and the ambient saltwater is prone to tilting due to the buoyancy effect (Figure 8), the dimensionless parameter *D* of Bakker (2010) was used as an additional parameter for scaling (Eq. 8). *D* is an expression for the severity of density effects in a mixed convective system. For a lower *D*, more influence of buoyancy on the freshwater body can be expected, yielding a lower *RE* of conventional ASR (Bakker, 2010):

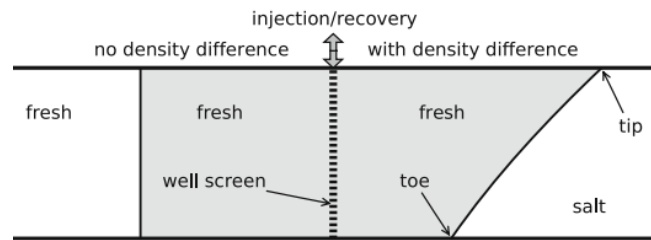
$$D = \frac{Q}{KvH^2} \quad \text{Eq. 8}$$

Where *v* is the relative density difference  $\frac{\rho_s - \rho_f}{\rho_f}$ , in which  $\rho_s$  is the density of ambient saline groundwater [M L<sup>-3</sup>] and  $\rho_f$  the density of the injected freshwater [M L<sup>-3</sup>].

Bakker (2010) stated that when mixing resulting from dispersion or diffusion is not considered, the radial velocity of the fresh-salt interface during pumping, and hence the quality of recovered water, is only governed by *D* and by the relative lengths of the injection, storage and recovery periods. The practical meaning of his findings is that injection for 10 days, storage for 5 days and recovery for 10 days results in the same *RE* as an ASR scenario of 100 days of injection, 50 days of storage and 100 days of recovery, provided that the same value of *D* is used. Therefore, the *RE* is not a function of the absolute duration of infiltration, storage and/or recovery.

### 2.6. *ASR scenarios*

Several scenarios were studied in this research to answer the research questions and to address the main hypothesis (Table 3). For a given ASR scenario, all models had the same values for *r/H* at the end of the infiltration phase (Eq. 6 and 7) and for *D* (Eq. 8). A reference scenario was simulated in the numerical models without variable density flow (Scenario 1) and with variable density flow (Scenario 2) to approximate the experimental dispersivity in the numerical models and to determine the effect of numerical dispersion. Scenario 3 was modelled with the ambient *TDS* concentration observed in the Westland area. Scenario 4 was modelled with twice the concentrations and pumping rates compared to Scenario 3 but with equal values for *D* and *r/H*. Several scenarios (Scenario 4 – 9) were also simulated with either a different *D*-value or a different *r/H*-value. This allowed to discuss the trends observed in the ASR-performance in terms of *D* and *r/H*. It also allowed to test and discuss the conclusion of Bakker (2010). Both FPW-ASR and MPPW-ASR were simulated for every scenario such that the improvement in the ASR performance could be determined in every model. Note again that for all scenarios, infiltration was simulated with a fully penetrating well and extraction in MPPW-ASR was simulated with a single partially penetrating well in the upper half of the aquifer for simplification. Therefore, the performance of MPPW-ASR was not necessarily optimised. The duration of the storage phase was equal to the duration of the infiltration phase, and equal pumping rates were used for extraction and infiltration. As a result, the relative durations of infiltration, storage and recovery were equal for every model and every scenario.



**Figure 8:** Vertical cross-section through an ASR-well. The left frame indicates the vertical interface between the injected and ambient water when there is no density difference. The right frame indicates the tilted interface when the density of the injected water is lower than that of the ambient water (Bakker, 2010).

**Table 3:** Scenarios studied in this research and the corresponding values for the parameters in the 3D-field model, the 2D-field model, the 2D-lab model, the 2D-filter model, and the experiments (models A, B, C, D and E, respectively; Figure 3).

Parameter	Setting	Model	Unit	Scenario*								
				1**	2	3	4	5	6	7	8	9
<b>Pumping rate (Q)</b>	Field	A,B	m <sup>3</sup> /d	600	600	300	600	600	400	400	1000	1000
	Lab	C,D,E	cm <sup>3</sup> /s	0.694	0.694	0.347	0.694	0.694	0.463	0.463	1.157	1.157
<b>Infiltration duration</b>	3D-field	A	d	3.57	3.57	7.14	3.57	1.587	5.355	2.38	2.142	0.952
	2D-field	B	d	2.5	2.5	5	2.5	1.667	3.75	2.5	1.5	1
	Lab	C,D,E	s	2160	2160	4320	2160	1440	3240	2160	1296	864
<b>Storage duration</b>	3D-field	A	d	3.57	3.57	7.14	3.57	1.587	5.355	2.38	2.142	0.952
	2D-field	B	d	2.5	2.5	5	2.5	1.667	3.75	2.5	1.5	1
	Lab	C,D,E	s	2160	2160	4320	2160	1440	3240	2160	1296	864
<b>Extraction duration</b>	3D-field	A	d	10.71	10.71	21.42	10.71	4.76	16.065	7.14	6.426	2.856
	2D-field	B	d	7.5	7.5	15	7.5	5	11.25	7.5	4.5	3
	Lab	C,D,E	s	6480	6480	12960	6480	4320	3240	6480	3888	2592
<b>Infiltrated volume of freshwater (V)</b>	3D-field	A	m <sup>3</sup>	2142	2142	2142	2142	952	2142	952	2142	952
	2D-field	B	m <sup>3</sup>	1500	1500	1500	1500	1000	1500	1000	1500	1000
	Lab	C,D,E	L	1.5	1.5	1.5	1.5	1	1.5	1	1.5	1
<b>Average radius of the freshwater body (r)</b>	Field	A,B	m	9.091	9.091	9.091	9.091	6.061	9.091	6.061	9.091	6.061
	Lab	C,D,E	cm	9.091	9.091	9.091	9.091	6.061	9.091	6.061	9.091	6.061
<b>Ambient TDS concentration (C<sub>amb</sub>)</b>	All	A,B,C,D,E	g/L	17.364	17.364	8.682	17.364	17.364	17.364	17.364	17.364	17.364
<b>Injected TDS concentration (C<sub>in</sub>)</b>	All	A,B,C,D,E	g/L	15.6276	15.6276	0.1	0.2	0.2	0.2	0.2	0.2	0.2
<b>Dimensionless parameters</b>												
<b>D (Bakker, 2010)</b>	All	A,B,C,D,E	-	∞	14.36	1.436	1.436	1.436	0.957	0.957	2.393	2.393
<b>r/H</b>	All	A,B,C,D,E	-	0.364	0.364	0.364	0.364	0.242	0.364	0.242	0.364	0.242
<b>Experiments</b>				-	√	-	√	√	√	√	√	√

\*The table represents the exact input parameters used to simulate the scenarios in SEAWAT. The amount of significant figures of these parameters is not applicable for the experiments, as they include measurement inaccuracies (Section 4.3.4).

\*\*Variable density flow was used in SEAWAT for all scenarios, except for scenario 1.

## 2.7. Metrics to quantify the results

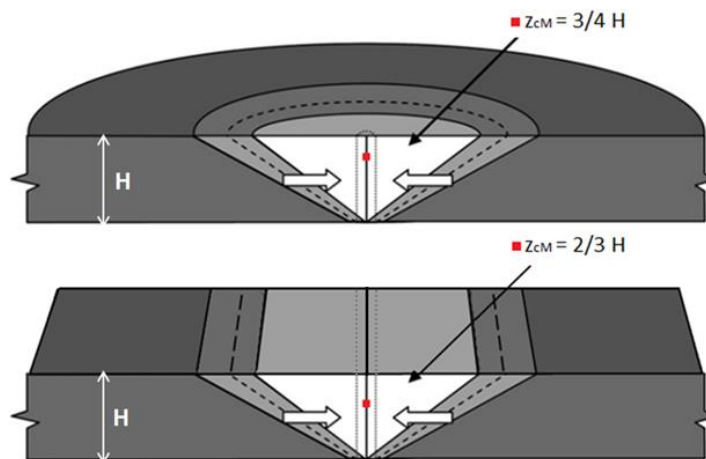
### 2.7.1. Dimensions of the freshwater body

Both the experimental and the numerical results of the different ASR scenarios were analysed at the end of the injection and storage phases on the basis of the dimensions of the freshwater body. The radius of the freshwater body at the top of the aquifer ( $r_{top}$ ) and at the bottom of the aquifer ( $r_{bottom}$ ) were documented (*Figure 8*). These were determined from the visible boundary of the blue tracer in the experiments, and from the 50% isochlor in the numerical simulations. The slope of the fresh-salt interface ( $\theta$ ) was computed as a ratio with the same equation as used by Ward et al. (2007) (*Eq. 9*). Note that  $\theta$  does not represent the angle of a slope here, as it often does in the literature.

$$\theta = \frac{r_{top} - r_{bottom}}{H} \quad \text{Eq. 9}$$

### 2.7.2. Vertical position of the centre of mass of freshwater ( $z_{cm}$ )

The vertical position of the centre of mass of freshwater ( $z_{cm}$ ) was determined for the representative 3D- and 2D-field settings on the basis of the dimensions of the freshwater body after the storage phase. This allowed to assess the discrepancy between a 3D ASR system with a normal fully penetrating well and a 2D ASR system with a planar fully penetrating well. The conical distribution of freshwater in a 3D-setting and the triangular distribution in a 2D-setting are displayed in *Figure 9* for the moment when the fresh-salt interface reaches the FPW-ASR well.



**Figure 9:** Distribution of freshwater for a vertical linear well with axis-symmetric flow patterns (top) and for a vertical planar well with 2D-flow patterns (bottom). The light colour represents the infiltrated freshwater and the darker colour indicates the ambient saltwater. The indicated vertical positions of the centres of mass ( $z_{cm}$ ; red) are for the moment when the 50% isochlor reaches the well at the bottom of the aquifer ( $r_{bottom} = 0$ ). The figure is adjusted from Ward et al. (2007).

When the fresh-salt interface does not reach the ASR-well yet, the distribution of freshwater resulting from ASR with a normal fully penetrating well in a 3D-setting is like a conical frustum, whereas the distribution resulting from ASR with a planar fully penetrating well in a 2D-setting is like a isosceles trapezoid. The vertical position of the centre of mass for the 3D-setting ( $z_{cm, 3D}$ ) was determined with *Eq. 10* (Beyer, 1987):

$$z_{cm, 3D} = \frac{h(r_{bottom}^2 + 2r_{bottom}r_{top} + 3r_{top}^2)}{4(r_{bottom}^2 + r_{bottom}r_{top} + r_{top}^2)} \quad \text{Eq. 10}$$

And for the 2D-setting ( $z_{cm, 2D}$ ), *Eq. 11* was used (Harris & Stöcker, 1998):

$$z_{cm, 2D} = \frac{h(r_{bottom} + 2r_{top})}{3(r_{bottom} + r_{top})} \quad \text{Eq. 11}$$

### 2.7.3. Mixing fraction ( $f(t)$ )

During the recovery phase in the experiments, the electrical conductance ( $EC$ ) of extracted water was continuously measured with a Tetracon 325 conductivity cell (Xylem Analytics, Germany) (Figure 1). These measurements were converted to  $TDS$ , after calibrating the relationship between both parameters. To keep track of the recovered  $TDS$  concentration during numerical simulations, concentration observation wells were placed in the middle of the extraction well. The average  $TDS$  concentration in all individual cells of the well during recovery was therefore assumed to be representative for the recovered water quality.

To overcome the issue of arbitrary threshold concentrations, the mixing fraction ( $f(t)$ ) was introduced by Pavelic et al. (2002) and Ward et al. (2007) as a parameter to determine the temporal behaviour of the recovered water quality.  $f(t)$  is defined as the proportion of injected water in the recovered water as a function of time during recovery (Eq. 12) (Pavelic et al., 2002; Ward et al., 2007):

$$f(t) = \frac{C_{amb} - C(t)}{C_{amb} - C_{in}} \quad \text{Eq. 12}$$

where  $C_{in}$  is the concentration of the infiltrated water,  $C_{amb}$  the concentration of the ambient groundwater, and  $C(t)$  the extracted concentration at time  $t$  in the recovery phase. When  $f(t)$  has a value of 1, the recovered water is of optimal quality. However, as the infiltrated water mixes with the ambient groundwater over time,  $f(t)$  decreases during recovery. Plotting the mixing fraction versus the fraction of recovery [-], i.e. the fraction of infiltrated water that is extracted, thus provides insight in the recovered water quality over time.

### 2.7.4. Recovery efficiency ( $RE$ )

To discuss the performance of ASR, the recovery efficiency ( $RE$ ) should be determined for a high mixing fraction, since recovered water should meet drinking water or irrigation water standards for most cases in practice. As a result, the  $RE$  was determined at an arbitrary mixing fraction threshold of 0.9 in this study. The absolute and relative difference between the  $RE$  of MPPW-ASR ( $RE_{MPPW}$ ) and that of FPW-ASR ( $RE_{FPW}$ ) were defined as  $\Delta RE$  (Eq. 13) and  $\%RE$  (Eq. 14), respectively. Both parameters were used in this study to determine the improved performance of MPPW-ASR compared to FPW-ASR.

$$\Delta RE = RE_{MPPW} - RE_{FPW} \quad \text{Eq. 13}$$

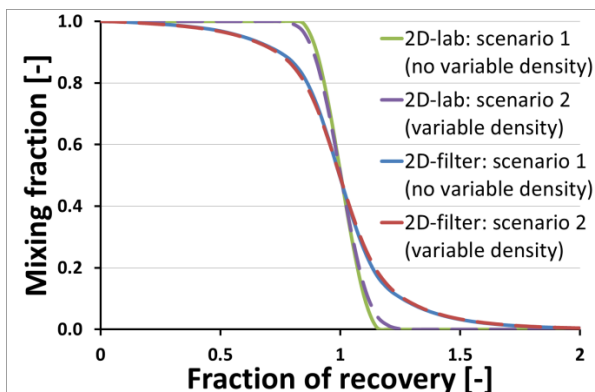
$$\%RE = \frac{RE_{MPPW} - RE_{FPW}}{RE_{FPW}} * 100 = \frac{\Delta RE}{RE_{FPW}} * 100 \quad \text{Eq. 14}$$

### 3. Results

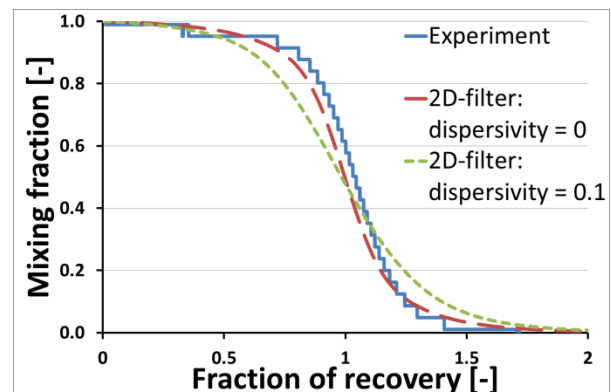
#### 3.1. Assessment of dispersivity

Before the numerical models were used to simulate the different ASR scenarios, the dispersivity was fitted with the experimental results. Since the experimental dispersivity ( $\alpha$ ) was unknown, the corresponding dispersivity for the numerical models was estimated on the basis of a reference scenario without variable density in SEAWAT (Scenario 1; Table 3). However, the effect of density could not be removed in the experimental set-up because the mixing fraction should be retrieved. Therefore, a comparable scenario was simulated with variable density flow in which the TDS concentration of infiltrated water was equal to 90% of the concentration in the ambient water (Scenario 2; Table 3). The root mean square error (RMSE) of the mixing fraction between both scenarios was equal to 0.010 for the 2D-lab model and to 0.004 for the 2D-filter model (Figure 10). The influence of density on the recovered concentration in Scenario 2 was thus assumed to be negligible. As a result, this scenario was used to fit the recovered mixing fraction in the numerical models with the experimental results by adjusting the specified dispersivity.

The recovered mixing fraction in the 2D-filter model corresponded best with the experiments if a dispersivity of 0 was specified for the numerical models (Figure 11). However, the transition of the mixing fraction was still too gradual in the 2D-filter model compared to the experimental results, which also seem to have a slight lag. Nevertheless, the remaining scenarios were simulated in the numerical models with a specified dispersivity of 0. The validity of this fitting strategy will be discussed in Section 4.1.



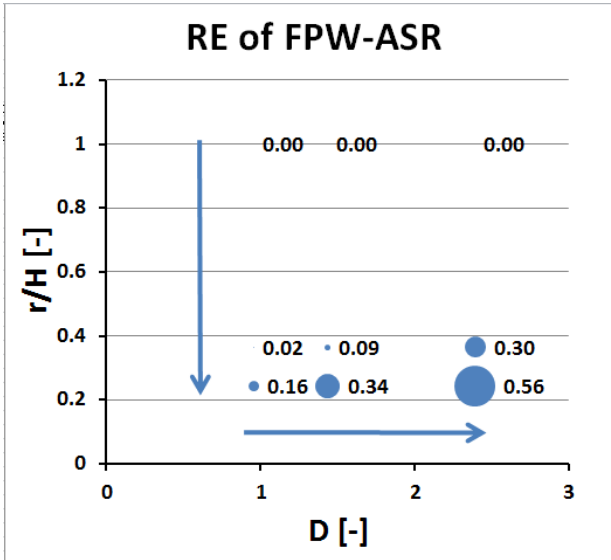
**Figure 10:** Comparison of Scenarios 1 (without variable density) and 2 (with variable density) for the numerical 2D-lab model (model C; Figure 3) and 2D-filter model (model D; Figure 3). The infiltrated concentration ( $C_{in}$ ) was equal to 90% of the ambient saltwater ( $C_{amb}$ ) and the specified dispersivity was 0.



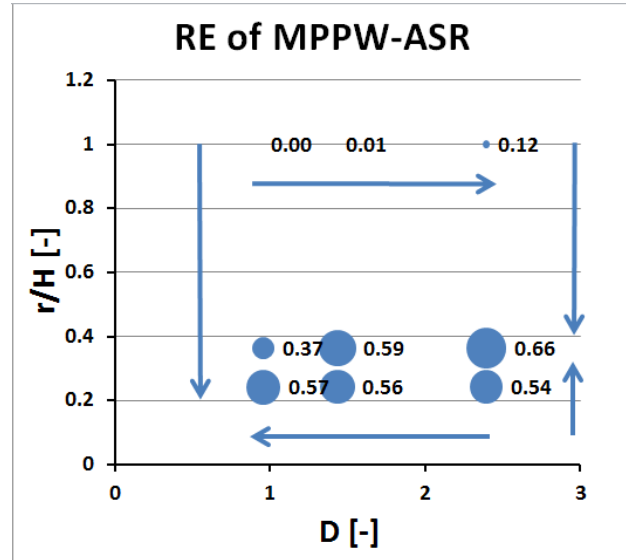
**Figure 11:** Comparison of the experimental results (model E; Figure 3) and the numerical 2D-filter model results (model D; Figure 3) for different specified dispersivity-values with use of Scenario 2 (Table 3). The dispersivity-values are given in cm.

### 3.2. ASR performance in the representative numerical 3D-field setting

The RE of FPW-ASR and MPPW-ASR is presented as a function of both  $D$  and  $r/H$  for the 3D-field model (model A; Figure 3) in Figure 12 and 13. This allowed to assess the performance of ASR with linear well screens in a representative field setting. In addition to the scenarios described in Section 2.6, three scenarios were simulated for the same  $D$ -values but with an  $r/H$  of 1. For this purpose, the distance to the constant head boundaries was increased by a factor of ten, which did not significantly affect the results of the other scenarios.



**Figure 12:** The RE of FPW-ASR presented as a function of both  $D$  and  $r/H$ . The size of the blue dots corresponds with the RE given by the neighbouring numbers. The blue arrows indicate the directions for which the RE increases.



**Figure 13:** The RE of MPPW-ASR presented as a function of both  $D$  and  $r/H$ . The size of the blue dots corresponds with the RE given by the neighbouring numbers. The blue arrows indicate the directions for which the RE increases.

The RE of FPW-ASR increased with a less significant buoyancy effect (a higher  $D$ ) and with a shorter duration of infiltration (a lower  $r/H$ ) (Figure 12). The RE is therefore controlled by both  $r/H$  and  $D$  and this control is unidirectional for FPW-ASR. The scenarios of FPW-ASR with an  $r/H$  of 1 resulted in a RE of 0, indicating that salinization of the well already occurred during the storage phase.

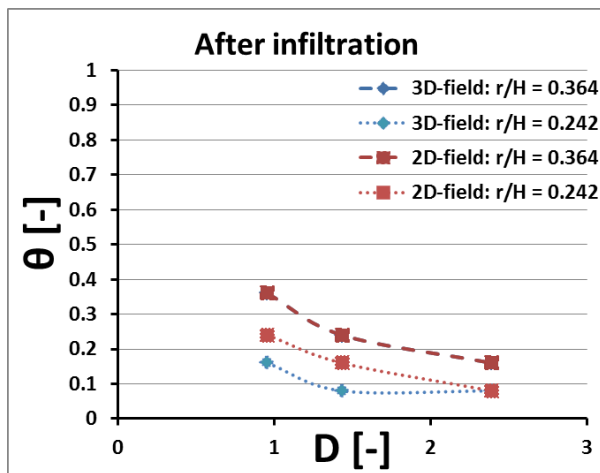
At a low  $r/H$  of 0.242, the RE of MPPW-ASR slightly increased with a lower  $D$  (Figure 13). However, for higher values of  $r/H$ , the RE of MPPW-ASR increased with a higher  $D$ , similar to the performance of FPW-ASR. The control of  $r/H$  and  $D$  on the RE of MPPW-ASR is therefore not unidirectional. In other words, the RE of MPPW-ASR has an optimum at a certain  $r/H$  for a given  $D$ . The RE of MPPW-ASR is larger than that of FPW-ASR for most situations.

### 3.3. Comparison of the numerical 3D- and 2D-field model results

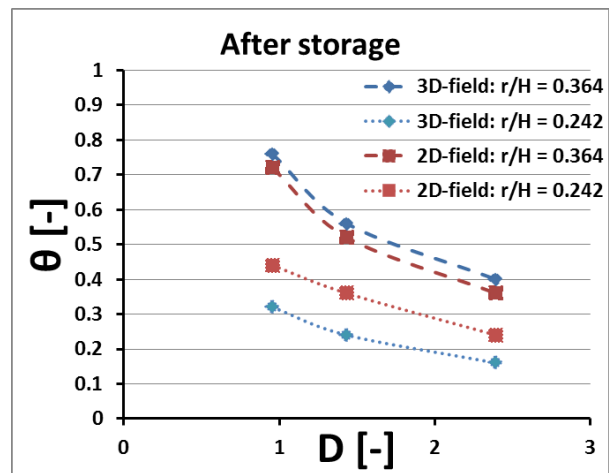
The results of the 3D-field model (model A; Figure 3) and the 2D-field model (model B; Figure 3) were compared in terms of  $D$  and  $r/H$ . This allowed to assess the scalability of individual 2D-models and 3D-models and the related ASR performance. In addition, it allowed to discuss the discrepancies introduced by the difference in nature between both settings.

#### 3.3.1. Slope of the fresh-salt interface ( $\theta$ ) in the numerical 3D- and 2D-field models

$\theta$  was plotted versus  $D$  for an  $r/H$  of 0.242 and 0.364 in the 3D-field model and the 2D-field model after infiltration (Figure 14) and after storage (Figure 15). The corresponding freshwater radii ( $r_{top}$  and  $r_{bottom}$ ) of Scenarios 4-9 are given in Appendix 7.2 and the overall shape of the freshwater body is graphically displayed in Appendix 7.3.



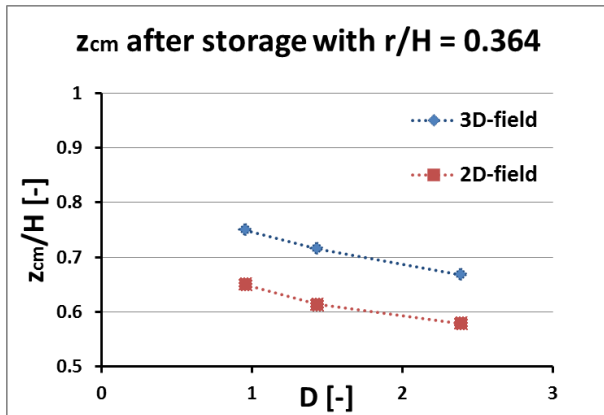
**Figure 14:** The slope of the fresh-salt interface ( $\theta$ ) after infiltration in the 3D-field model (model A; Figure 3) and the 2D-field model (model B; Figure 3) plotted versus  $D$  for an  $r/H$  of 0.364 and an  $r/H$  of 0.242. Note that the results of the 3D-field model are exactly equal to the 2D-field model for an  $r/H$  of 0.364.



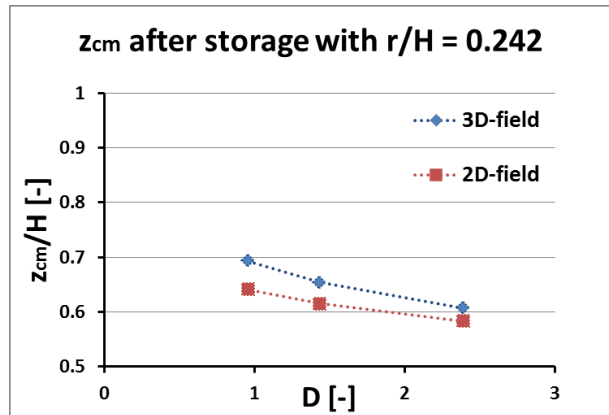
**Figure 15:** The slope of the fresh-salt interface ( $\theta$ ) after storage in the 3D-field model (model A; Figure 3) and the 2D-field model (model B; Figure 3) plotted versus  $D$  for an  $r/H$  of 0.364 and an  $r/H$  of 0.242.

The results confirm that  $\theta$  increased during the storage phase. Moreover, the results indicate that  $\theta$  is higher with a more significant buoyancy effect (a lower  $D$ ) and with a higher  $r/H$ . For an  $r/H$  of 0.364,  $\theta$  was approximately equal in both models, whereas  $\theta$  was higher in the 2D-field model compared to the 3D-field model for an  $r/H$  of 0.242. The shape of the freshwater body in the 3D-field model was therefore not consistently transferrable to the 2D-field model by only using  $D$  and  $r/H$  as scaling parameters.

3.3.2. Vertical position of the centre of mass ( $z_{cm}$ ) in the numerical 3D- and 2D-field models  
 $z_{cm, 3D}$  and  $z_{cm, 2D}$  (Eq. 10 and 11) are given in Appendix 7.4 for Scenarios 4 – 9 in the numerical 3D- and 2D-field models. They were plotted versus  $D$  relative to  $H$  for an  $r/H$  of 0.364 and 0.242 after storage (Figure 16 and 17).



**Figure 16:** Vertical position of the centre of mass of freshwater relative to the thickness of the aquifer ( $z_{cm}/H$ ) plotted versus  $D$  for an  $r/H$  of 0.364 in the representative numerical 3D- and 2D-field models.



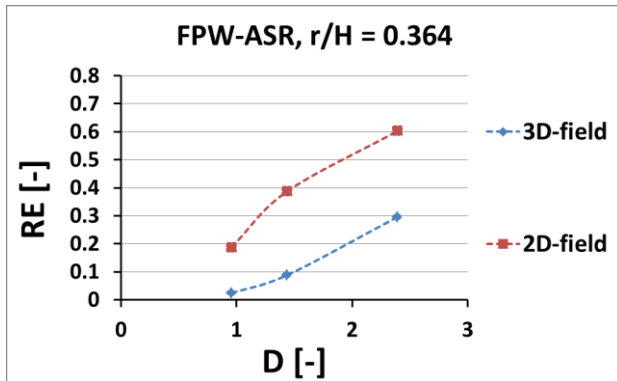
**Figure 17:** Vertical position of the centre of mass of freshwater relative to the thickness of the aquifer ( $z_{cm}/H$ ) plotted versus  $D$  for an  $r/H$  of 0.242 in the representative numerical 3D- and 2D-field models.

$z_{cm}/H$  was higher than 0.5 because more freshwater was situated in the upper half of the aquifer compared to the lower half. It decreased with an increasing  $D$ . The difference between  $z_{cm}$  in the 3D-field model and the 2D-field model was relatively larger in the simulations with  $r/H = 0.364$  compared to the simulations with  $r/H = 0.242$ . The vertical distribution of freshwater in a 3D-aquifer was therefore not consistently transferrable to a 2D-aquifer by only using  $D$  and  $r/H$  as scaling parameters.

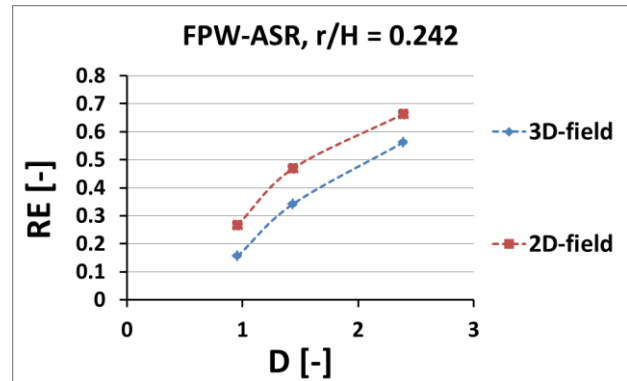


3.3.3. Recovery efficiency (RE) in the numerical 3D- and 2D-field models

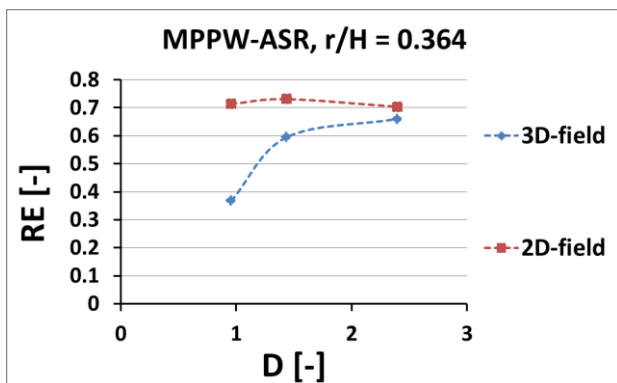
The mixing fractions for Scenarios 3 – 9 in the 3D-field model and the 2D-field model are presented versus the fraction of recovery in *Appendix 7.5*. The corresponding RE-values for a mixing fraction of 0.9 are given in *Appendix 7.2* and are presented versus  $D$  for both FPW-ASR and MPPW-ASR and for an  $r/H$  of 0.364 and 0.242 in *Figure 18 – 21*. The results of  $\Delta RE$  (Eq. 13) are given in *Figure 22*.



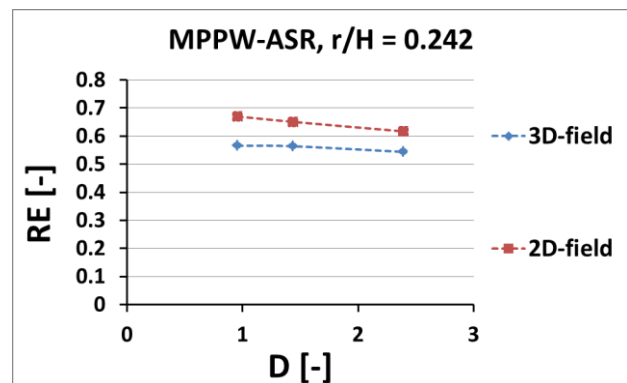
**Figure 18:** The RE of FPW-ASR in the 3D-field model (model A; Figure 3) and the 2D-field model (model B; Figure 3) plotted versus  $D$  for an  $r/H$  of 0.364.



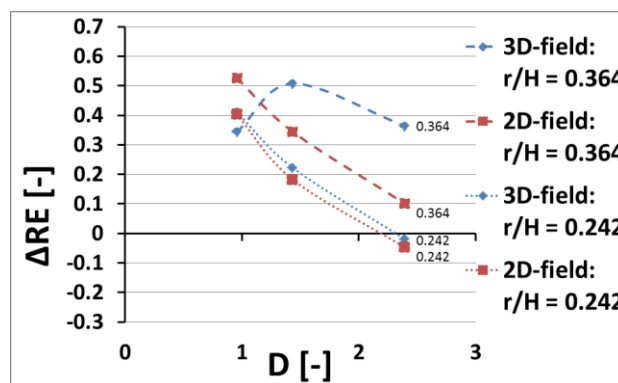
**Figure 19:** The RE of FPW-ASR in the 3D-field model (model A; Figure 3) and the 2D-field model (model B; Figure 3) plotted versus  $D$  for an  $r/H$  of 0.242.



**Figure 20:** The RE of MPPW-ASR in the 3D-field model (model A; Figure 3) and the 2D-field model (model B; Figure 3) plotted versus  $D$  for an  $r/H$  of 0.364.



**Figure 21:** The RE of MPPW-ASR in the 3D-field model (model A; Figure 3) and the 2D-field model (model B; Figure 3) plotted versus  $D$  for an  $r/H$  of 0.242.



**Figure 22:**  $\Delta RE$ , i.e. the absolute difference between the RE of MPPW-ASR and of FPW-ASR, in the 3D-field model (model A; Figure 3) and the 2D-field model (model B; Figure 3) plotted versus  $D$  for  $r/H = 0.364$  and for  $r/H = 0.242$ . The numbers in the graph indicate the corresponding  $r/H$ -values.

The lower  $RE$  of FPW-ASR with a more significant buoyancy effect (a lower  $D$ ) was confirmed in the 2D-field setting (*Figure 18* and *19*). The lower  $RE$  of MPPW-ASR with a higher  $D$  and a low  $r/H$  of 0.242 was also evident in the 2D-field model (*Figure 21*). However, the decrease of the  $RE$  of MPPW-ASR for a lower  $D$  and a higher  $r/H$  was less significant in the 2D-field model compared to the 3D-field model (*Figure 20*).

The  $RE$  of both FPW-ASR and MPPW-ASR was higher for the 2D-field model compared to the 3D-field model. The 2D-field model thus gave a too optimistic image of the actual  $RE$  that could be obtained in 3D-situations in the field.

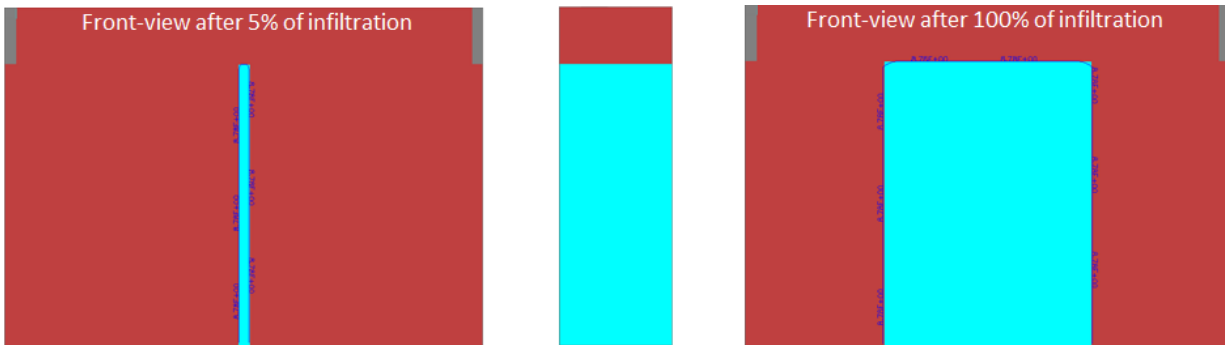
The positive values for the resulting  $\Delta RE$  indicate that the  $RE$  generally improved when MPPW-ASR was used instead of FPW-ASR (*Figure 22*). However, because  $\Delta RE$  was generally lower for a lower  $r/H$  and for a higher  $D$ ,  $\Delta RE$  was negative for a high  $D$  and a low  $r/H$ . Although  $\Delta RE$  was quite similar for both models with an  $r/H$  of 0.242,  $\Delta RE$  was generally lower for the 2D-field model compared to the 3D-field model. The exception to both statements was  $\Delta RE$  in the 3D-field model with an  $r/H$  of 0.364, for which  $\Delta RE$  first increased and later decreased with an increasing  $D$ . All these results indicate that the  $RE$  and the resulting  $\Delta RE$  depend on both  $D$  and  $r/H$  and that the results of the 2D-field model and the 3D-field model do not correspond when scaling is only based on the dimensionless parameters  $D$  and  $r/H$  and on the relative durations of infiltration, storage, and recovery.

### 3.4. Comparison of the numerical 2D-lab and 2D-filter model results

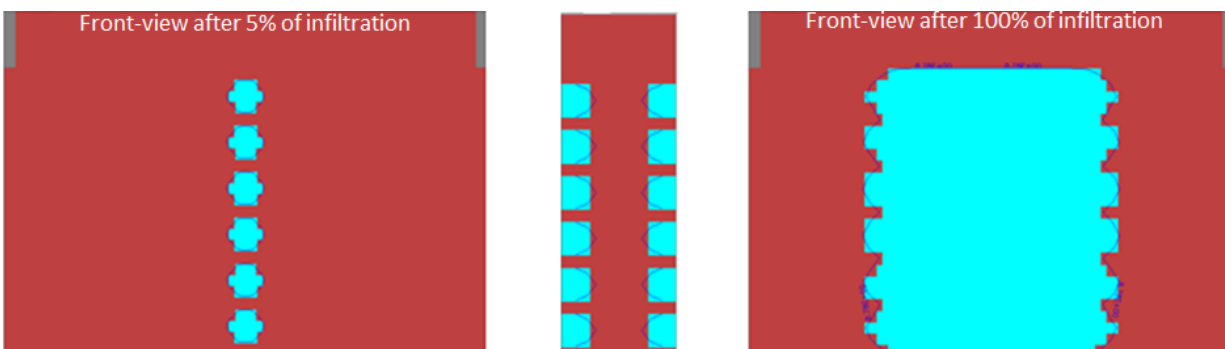
The results of the 2D-lab model (model C; Figure 3) and the 2D-filter model (model D; Figure 3) were compared in terms of  $D$  and  $r/H$ . This allowed to assess the scalability of individual 2D-models and the related ASR performance. It also allowed to discuss the discrepancies introduced by the well configuration.

#### 3.4.1. *Infiltration behaviour of a vertical planar well and of individual filter screens*

The ASR well was a planar fully penetrating well in the 2D-lab model, whereas it consisted of multiple individual filter screens in the 2D-filter model (Figure 5 and 6). The resulting infiltration patterns in both models are indicated in Figure 23 and 24.



**Figure 23:** Infiltration pattern for the 2D-lab model (model C; Figure 3) without variable density flow (Scenario 1; Table 3). The middle frame represents the vertical cross-section through the well perpendicular to the left frame after 5% of infiltration. The boundary between the blue and red colours represents the 50% isochlor.



**Figure 24:** Infiltration pattern for the 2D-filter model (model D; Figure 3) without variable density flow (Scenario 1; Table 3). The middle frame represents the vertical cross-section through the well perpendicular to the left frame after 5% of infiltration. The boundary between the blue and red colours represents the 50% isochlor.

These cross-sections indicate that the 2D-filter model (Figure 24) did not represent a single infiltration source like the 2D-lab model did (Figure 23). Infiltration from the individual filter screens was rather characterized by separate freshwater bodies that merged during infiltration. Consequently, the fringe between the infiltrated freshwater and the ambient saltwater resulting from the individual filter screens was irregular, whereas the interface resulting from a vertical planar well was smooth and undisturbed.

3.4.2. Slope of the fresh-salt interface ( $\theta$ ) in the numerical 2D-lab and 2D-filter models

$\theta$  was plotted versus  $D$  for an  $r/H$  of 0.242 and 0.364 in the 2D-lab model and the 2D-filter model after infiltration (Figure 25) and after storage (Figure 26). The corresponding freshwater radii ( $r_{top}$  and  $r_{bottom}$ ) of Scenarios 4 – 9 are given in Appendix 7.2 and the overall shape of the freshwater body is graphically displayed in Appendix 7.3.

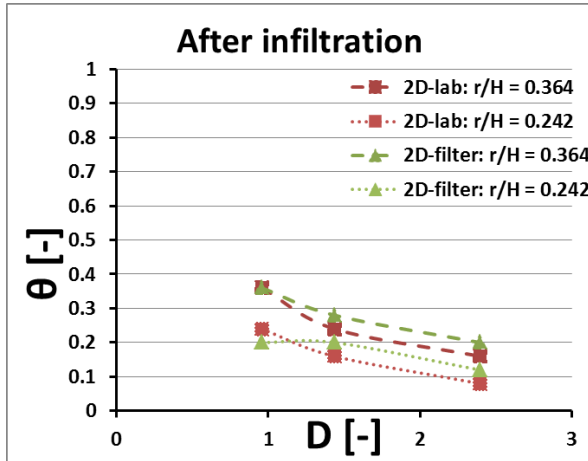


Figure 25: The slope of the fresh-salt interface ( $\theta$ ) after infiltration for the 2D-lab model (model C; Figure 3) and the 2D-filter model (model D; Figure 3) plotted versus  $D$  for an  $r/H$  of 0.364 and an  $r/H$  of 0.242.

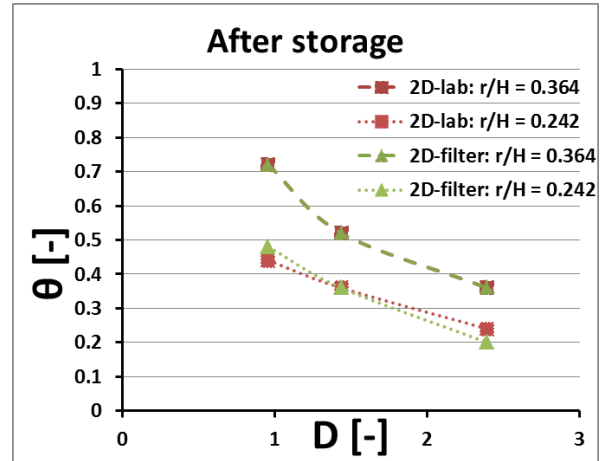


Figure 26: The slope of the fresh-salt interface ( $\theta$ ) after storage for the 2D-lab model (model C; Figure 3) and the 2D-filter model (model D; Figure 3) plotted versus  $D$  for an  $r/H$  of 0.364 and an  $r/H$  of 0.242.

These results confirm that  $\theta$  increased during the storage phase and that it was lower for a higher  $D$  and for a lower  $r/H$  in both the 2D-lab and the 2D-filter models. The value of  $\theta$  was approximately similar in both models, especially after storage. This indicates that the application of individual filter screens might be a representative substitute for a vertical planar well in the experimental set-up, at least with regard to the general morphology of the freshwater body.

3.4.3. Recovery efficiency (RE) in the numerical 2D-lab and 2D-filter models

The mixing fraction for Scenarios 3 – 9 in the 2D-lab model and the 2D-filter model are presented versus the fraction of recovery in Appendix 7.5. The corresponding RE-values for a mixing fraction of 0.9 are given in Appendix 7.2 and are presented versus  $D$  for both FPW-ASR and MPPW-ASR and for an  $r/H$  of 0.364 and 0.242 in Figure 27 – 30 . The results of  $\Delta RE$  (Eq. 13) are given in Figure 31.

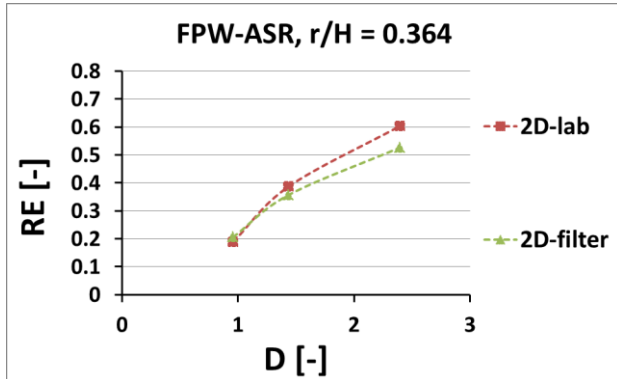


Figure 27: The RE of FPW-ASR in the 2D-lab model (model C; Figure 3) and the 2D-filter model (model D; Figure 3) plotted versus  $D$  for an  $r/H$  of 0.364.

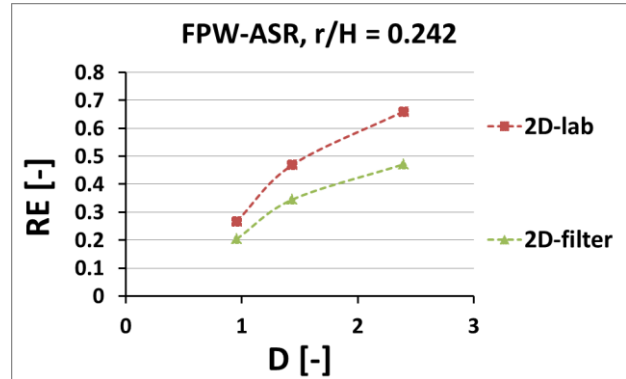


Figure 28: The RE of FPW-ASR in the 2D-lab model (model C; Figure 3) and the 2D-filter model (model D; Figure 3) plotted versus  $D$  for an  $r/H$  of 0.242.

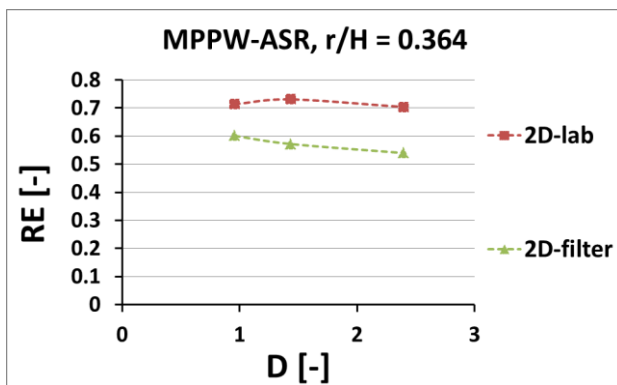


Figure 29: The RE of MPPW-ASR in the 2D-lab model (model C; Figure 3) and the 2D-filter model (model D; Figure 3) plotted versus  $D$  for an  $r/H$  of 0.364.

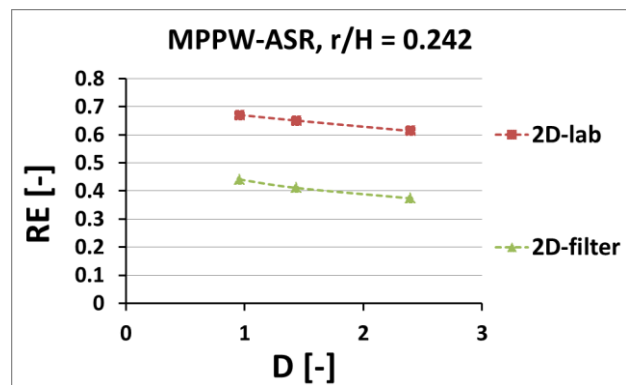


Figure 30: The RE of MPPW-ASR in the 2D-lab model (model C; Figure 3) and the 2D-filter model (model D; Figure 3) plotted versus  $D$  for an  $r/H$  of 0.242.

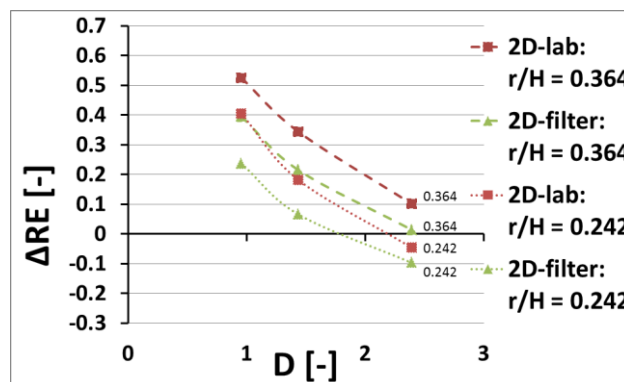


Figure 31:  $\Delta RE$ , i.e. the absolute difference between the RE of MPPW-ASR and of FPW-ASR, in the 2D-lab model (model C; Figure 3) and the 2D-filter model (model D; Figure 3) plotted versus  $D$  for  $r/H = 0.364$  and for  $r/H = 0.242$ . The numbers in the graph indicate the corresponding  $r/H$ -values.

The lower  $RE$  for FPW-ASR with a decreasing  $D$  and for MPPW-ASR with an increasing  $D$  was also evident in these two lab-models (*Figure 27 – 30*). The  $RE$  was, however, lower for the 2D-filter model compared to the 2D-lab model, especially with MPPW-ASR. The potential  $RE$  is therefore underestimated when individual filter screens are applied as a representation of a vertical planar well. The  $RE$  in the 2D-filter model corresponded better with the  $RE$  in the 2D-lab model with a longer duration of infiltration (a higher  $r/H$ ). Moreover, the  $RE$  for FPW-ASR in the 2D-filter model corresponded better with that of the 2D-lab model at a lower  $D$ .

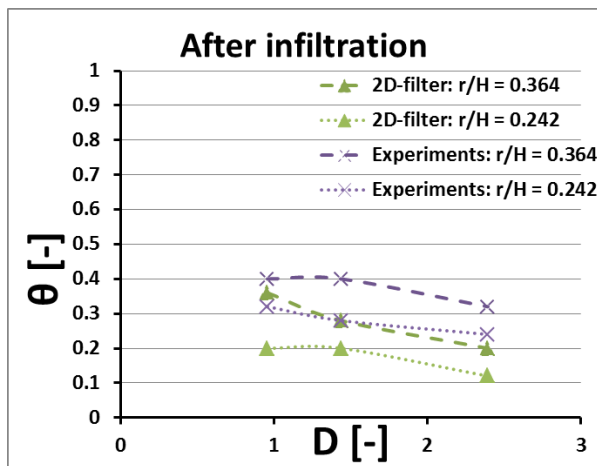
The positive values for  $\Delta RE$  confirm that the  $RE$  generally improved when MPPW-ASR was used instead of FPW-ASR in the numerical lab-scale models (*Figure 31*). The exception to this rule was again the negative  $\Delta RE$  for a high  $D$  and a low  $r/H$ . The decrease of  $\Delta RE$  with a lower  $r/H$  and a higher  $D$  was also evident in these two models. However,  $\Delta RE$  was consistently lower for the 2D-filter model compared to the 2D-lab model, indicating that the individual filter screens cause the experiments to underestimate the  $\Delta RE$  that can be achieved with a fully penetrating planar well.

### 3.5. Comparison of the numerical 2D-filter model and the experimental results

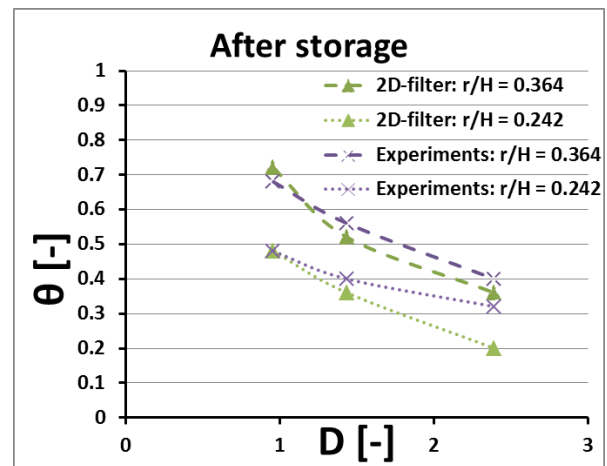
The results of the 2D-filter model (model D; Figure 3) and the experiments (model E; Figure 3) were compared in terms of  $D$  and  $r/H$ . This allowed to assess the ASR performance and to discuss the discrepancies between physical modelling and numerical modelling.

#### 3.5.1. Slope of the fresh-salt interface ( $\theta$ ) in the numerical 2D-filter model and the experiments

$\theta$  was plotted versus  $D$  for an  $r/H$  of 0.242 and 0.364 in the 2D-filter model and in the experiments after infiltration (Figure 32) and after storage (Figure 33). The corresponding freshwater radii ( $r_{top}$  and  $r_{bottom}$ ) of Scenarios 4-9 are given in Appendix 7.2 and the overall shape of the freshwater body is graphically displayed in Appendix 7.3. The infiltration pattern without a significant buoyancy effect is visualised in Appendix 7.6 (Scenario 2) and a typical experimental ASR scenario is visualized in Appendix 7.7 (Scenario 4).



**Figure 32:** The slope of the fresh-salt interface ( $\theta$ ) after infiltration for the 2D-filter model (model D; Figure 3) and the experiments (model E; Figure 3) plotted versus  $D$  for an  $r/H$  of 0.364 and an  $r/H$  of 0.242.



**Figure 33:** The slope of the fresh-salt interface ( $\theta$ ) after storage for the 2D-filter model (model D; Figure 3) and the experiments (model E; Figure 3) plotted versus  $D$  for an  $r/H$  of 0.364 and an  $r/H$  of 0.242.

These results indicate that  $\theta$  also increased during the storage period in the experiments. The lower  $\theta$  for a higher  $D$  and for a lower  $r/H$  was also evident in the experiments. However,  $\theta$  was higher in the experiments compared to the numerical 2D-filter model. This indicates that the numerical model was not completely representative for the experiments. However, the offset generally decreased during the storage period and with a lower  $D$ . The infiltration pattern in Appendix 7.6 suggests that the experimental well configuration infiltrates water preferentially in the top of the aquifer.

3.5.2. Recovery efficiency (RE) in the numerical 2D-filter model and the experiments

The mixing fraction for Scenarios 3 – 9 in the 2D-filter model and the experiments are presented versus the fraction of recovery in Appendix 7.5. The corresponding RE-values for a mixing fraction of 0.9 are given in Appendix 7.2 and are presented versus  $D$  for both FPW-ASR and MPPW-ASR and for an  $r/H$  of 0.364 and 0.242 in Figure 34 – 37. The results of  $\Delta RE$  (Eq. 13) are given in Figure 38.

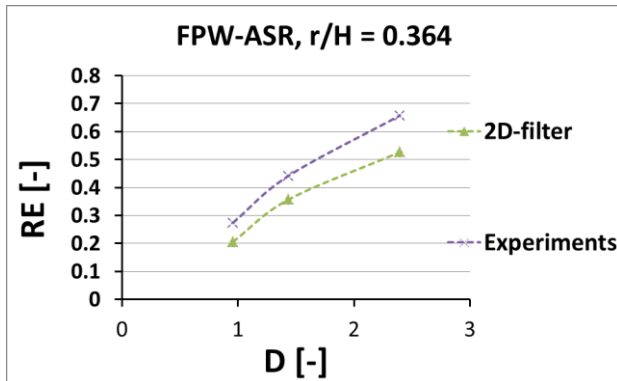


Figure 34: The RE of FPW-ASR in the 2D-filter model (model D; Figure 3) and the experiments (model E; Figure 3) plotted versus  $D$  for an  $r/H$  of 0.364.

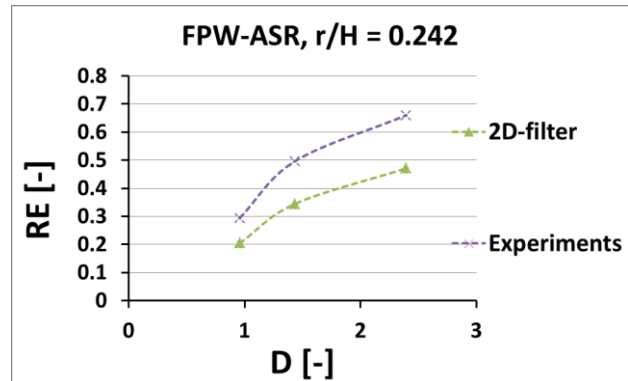


Figure 35: The RE of FPW-ASR in the 2D-filter model (model D; Figure 3) and the experiments (model E; Figure 3) plotted versus  $D$  for an  $r/H$  of 0.242.

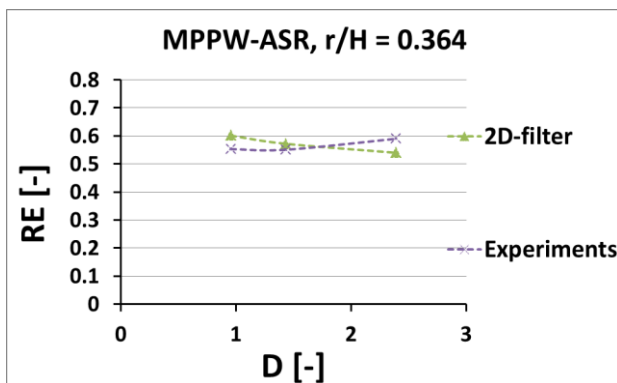


Figure 36: The RE of MPPW-ASR in the 2D-filter model (model D; Figure 3) and the experiments (model E; Figure 3) plotted versus  $D$  for an  $r/H$  of 0.364.

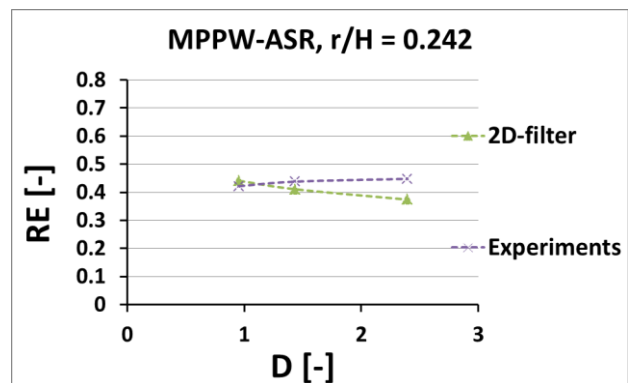


Figure 37: The RE of MPPW-ASR in the 2D-filter model (model D; Figure 3) and the experiments (model E; Figure 3) plotted versus  $D$  for an  $r/H$  of 0.242.

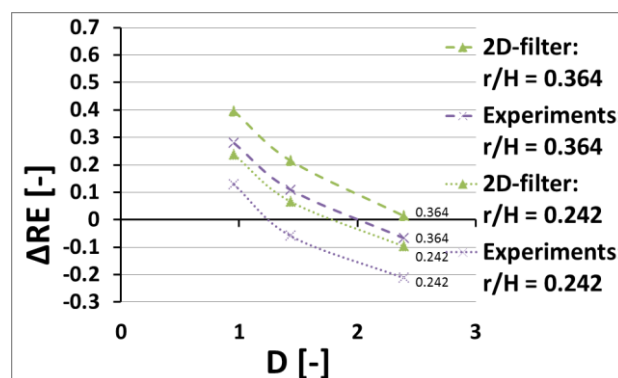


Figure 38:  $\Delta RE$ , i.e. the absolute difference between the RE of MPPW-ASR and of FPW-ASR, in the 2D-filter model (model D; Figure 3) and the experiments (model E; Figure 3) plotted versus  $D$  for  $r/H = 0.364$  and for  $r/H = 0.242$ . The numbers in the graph indicate the corresponding  $r/H$ -values.

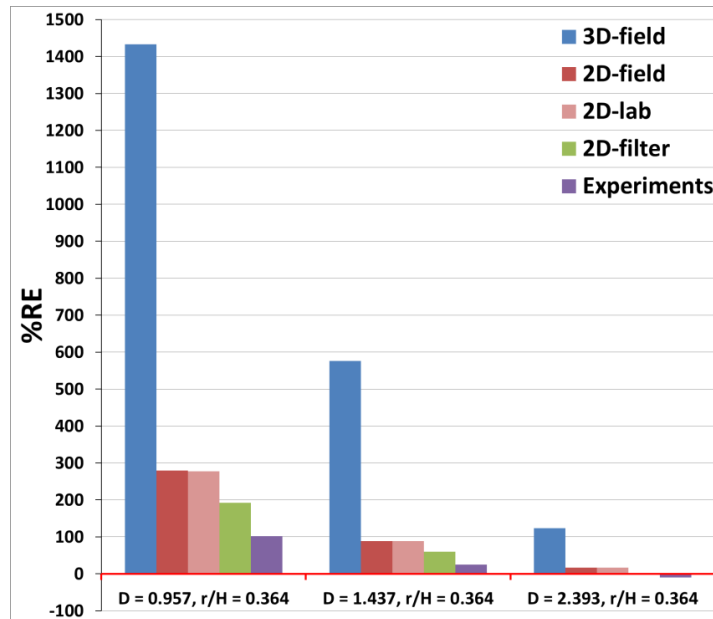


The lower  $RE$  for FPW-ASR with a lower  $D$  was also evident in the experiments (Figure 34 and 35). The  $RE$  of FPW-ASR was, however, higher in the experiments compared to the 2D-lab model. This offset appeared to decrease with a decreasing  $D$ . The  $RE$  of MPPW-ASR was similar in both models (Figure 36 and 37). However, it decreased gently with an increasing  $D$  for the 2D-filter model, whereas it slightly increased in the experiments.

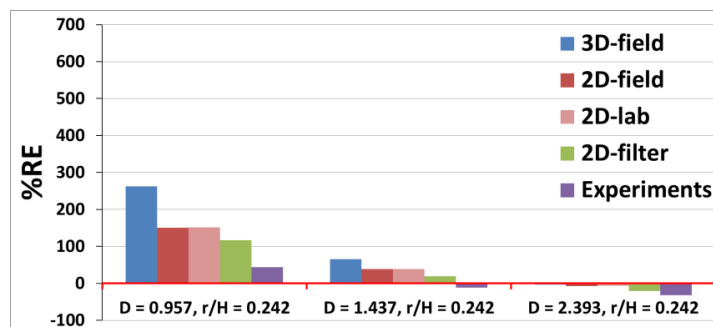
The positive values for the resulting  $\Delta RE$  indicate that the  $RE$  also generally improved when MPPW-ASR was used instead of FPW-ASR in the experiments (Figure 38). The exception to this rule was again the negative  $\Delta RE$  for a high  $D$  and a low  $r/H$ . On top of this, the  $\Delta RE$  was consistently lower for the experiments compared to the 2D-filter model, causing the experimental  $\Delta RE$  to be also negative for a  $D$  of 1.437 and an  $r/H$  of 0.242, and for a  $D$  of 2.393 and an  $r/H$  of 0.364. Nevertheless, the trend of a decreasing  $\Delta RE$  with a lower  $r/H$  and a higher  $D$  was evident in all 2D-models.

### 3.6. Relative ASR performance of MPPW-ASR compared to FPW-ASR (%RE)

The %RE was plotted versus  $D$  for every model for an  $r/H$  of 0.364 (Figure 39) and for an  $r/H$  of 0.242 (Figure 40). The trends observed in these results complement the insights gained from the trends in  $\Delta RE$ .



**Figure 39:** %RE in the five different models used in this research (Figure 3) plotted versus  $D$  for an  $r/H$  of 0.364. Positive values indicate that MPPW-ASR is more efficient than FPW-ASR.



**Figure 40:** %RE in the five different models used in this research (Figure 3) plotted versus  $D$  for an  $r/H$  of 0.242. Positive values indicate that MPPW-ASR is more efficient than FPW-ASR.

The general positive values of %RE indicate that the RE generally improved when MPPW-ASR was used instead of FPW-ASR. However, %RE decreased with an increasing  $D$  and with a decreasing  $r/H$ . As a result, all models indicate that the RE of MPPW-ASR was lower than the RE of FPW-ASR for a  $D$  of 2.393 and an  $r/H$  of 0.242 (negative %RE). Moreover, %RE was larger for the 3D-field model compared to that of the 2D-field model and the 2D-lab model. These 2D-settings with a vertical planar well resulted in equal values of %RE, which were higher than %RE resulting from using individual filter screens (2D-filter model) for all scenarios. The numerical 2D-filter model resulted in higher values of %RE compared to the experiments. The experiments even resulted in a worse performance of MPPW-ASR compared to FPW-ASR for a  $D$  of 1.437 and an  $r/H$  of 0.242 and for a  $D$  of 2.393 and an  $r/H$  of 0.364 (negative %RE), where the numerical models suggested a better performance of MPPW-ASR compared to FPW-ASR.

## 4. Discussion

### 4.1. Assessment of dispersivity

Although the specified dispersivity was 0 for the numerical results in *Figure 10*, the mixing fraction did not instantaneously change from 1 to 0 during recovery in the 2D-lab model. The gradual transition was the result of numerical dispersion, since molecular diffusion into the bentonite clay layer was negligible in the numerical simulations. The more gradual transition in the 2D-filter model was the result of increased mixing that occurred during infiltration and extraction in between the individual filter screens (*Figure 23 and 24*).

It was expected that the experimental dispersivity lied approximately within the range of 0.1 mm – 1 mm, i.e. corresponding with a rough estimate of the grain diameter (Goswami & Clement, 2007; Abarca & Clement, 2009; Luyun et al., 2011). However, the numerical results of the 2D-filter model corresponded best with the experimental results with a specified dispersivity of 0 because of the major influence of numerical dispersion (*Figure 11*).

It is rather arbitrary to fit the numerical models with the experimental results by adjusting the dispersivity when numerical dispersion is involved. Actual dispersion depends on the scale and the groundwater velocity, whereas numerical dispersion is introduced by the discretization of the grid used in numerical models. Because of this difference in nature, there is no scientific relationship between numerical and experimental dispersion. As a result, the actual effect of the experimental dispersivity could not be determined from the numerical models in this study. It could be determined more efficiently if numerical dispersion would have been negligible. Therefore, it is preferred to minimize numerical dispersion in SEAWAT simulations by using a finer grid discretization. However, the grid was not further refined in this study because no significant change was observed in the results by doubling the amount of cells. In addition, further refinement of the 3D-field model resulted in impractically long computation times, ranging from hours to days. Although the fitting procedure is not scientifically correct, it was considered to be acceptable for gaining insight in the general ASR performance for different scenarios. Addressing the main hypothesis with use of the numerical models is therefore still possible. As a result, using a specified dispersivity of 0 in the numerical model simulations was the best option given the findings in *Section 3.1* and the dispersivity was not further assessed in this study.

### 4.2. Influence of aquifer properties and operational parameters on the RE

This section deals with the first research question, which was stated as:

*'How do the aquifer properties and operational parameters influence the RE of FPW-ASR and MPPW-ASR, and which of these controlling parameters are scalable to what extent?'*

The effect of the aquifer properties and operational parameters on the *RE* of conventional ASR in the representative field setting is explained in *Section 4.2.1*. This section also deals with the scalability of the controlling parameters for different ASR scenarios, including a comparison with the results of Bakker (2010). In *Section 4.2.2* the effect of the controlling parameters on the performance of MPPW-ASR in the representative field setting is discussed.

#### 4.2.1. Influence of aquifer properties and operational parameters on the RE of FPW-ASR

The reduced *RE* of FPW-ASR in the representative field setting with an increased significance of the buoyancy effect (a lower  $D$ ) (*Figure 12*) was also evident from the results of Bakker (2010). This is caused by the steeper slope of the fresh-salt interface (*Figure 14 and 15*), resulting in a higher  $z_{cm}$  (*Figure 16 and 17*) and an earlier extraction of ambient saline groundwater. Considering the controlling parameters of  $D$  (*Eq. 8*), the *RE* of FPW-ASR is thus lower with a lower pumping rate ( $Q$ ), a larger density difference ( $\nu$ ), a higher hydraulic

conductivity ( $K$ ), and a thicker aquifer ( $H$ ) for a given duration of infiltration (e.g. Merritt, 1986; Ward et al., 2007; 2008; Zuurbier et al., 2013; Van Ginkel et al., 2014).

The lower  $RE$  of FPW-ASR for a larger infiltration volume (a higher  $r/H$ ) might be counterintuitive (Figure 12). However, this is also related to the buoyancy effect. For each  $D$ , the different infiltration volumes and  $r/H$ -values were obtained with equal pumping rates but by changing the duration of infiltration. The fresh-salt interface has more time to tilt with an increased duration of infiltration, and hence storage. This leads to a higher  $\theta$ , a higher  $z_{cm, 3D}$ , and thus to a more significant buoyancy effect (Figure 14 - 17). If the infiltration volume and  $r/H$  were increased by increasing  $Q$  instead of  $t$ ,  $D$  would also increase, leading to a less significant buoyancy effect, less interface tilting, and a higher  $RE$  of FPW-ASR.

These findings contradict the theory of Bakker (2010), who stated that the  $RE$  of ASR is only governed by  $D$  and by the relative durations of infiltration, storage, and recovery. Thus, the  $RE$  should be independent of  $r/H$ , i.e. the absolute duration of infiltration. The study of Bakker (2010) was also contradicted on the basis of the absolute  $RE$ . For equal durations of injection and storage, he documented a  $RE$  below 10% for scenarios with a  $D$  lower than 10. Although the ranges of aquifer properties and operational parameters studied here fell within the range of Bakker (2010), the resulting  $RE$  of FPW-ASR in the 3D-field model was about 30% for a  $D$  of 2.393 and an  $r/H$  of 0.364 (Figure 18).

The first contributor to these contradictions is the difference in the definition of  $RE$ , since Bakker (2010) defined the  $RE$  as the fraction of infiltrated water that is recovered before the fresh-salt interface reaches the ASR-well. In addition, the present research focused on relatively low  $D$ -values ranging between 0.9 and 2.4. Bakker (2010) confirmed his theory for a relatively small influence of buoyancy. However, he did not present his results for scenarios with a  $D$  below 10 for equal durations of infiltration and storage, possibly because his interface solution including the Dupuit and Boussinesq-Oberbeck approximations is not valid for such a large influence of buoyancy. On top of this, the  $D$ -parameter of Bakker (2010) assumes a sharp interface between ambient saltwater and infiltrated freshwater. However, Ward et al. (2009) and Barker et al. (2016) indicated that a higher dispersivity relative to the radius of the infiltrated freshwater body leads to poor ASR performance. On the other hand, Ward et al. (2007) stated that a wider dispersive zone would attenuate interface tilting. Although the nature of numerical dispersion is not comparable to that of actual dispersion, the numerical dispersion introduced in the simulations of this study also contributes to the contradiction. Bakker (2010) compared his results with a scenario simulated by Ward et al. (2008) including (numerical) dispersion and also attributed the resulting discrepancies in the  $RE$  to mixing resulting from (numerical) dispersion. The infiltration volumes studied in this research are relatively small compared to those studied by Bakker (2010). As a result, the importance of mixing by (numerical) dispersion is relatively large compared to the importance of the buoyancy effect and is expected to be larger for a lower  $r/H$ . For the relatively high  $r/H$  of 1, the  $RE$  already corresponded better with that of Bakker (2010), possibly due to a reduced relative influence of numerical dispersion. The effect of numerical dispersion may therefore not be transferrable to ASR scenarios with a different  $r/H$ . As a result, the conclusion of Bakker (2010) may be valid when numerical dispersion is not involved. However, no definite conclusions can be drawn on the basis of this study and the relationship between  $RE$  and  $r/H$  requires further research.

Nevertheless, this study suggests that the  $RE$  of ASR-scenarios in a numerical 3D-setting with different operational parameters in aquifers with different properties can be equal with the same  $D$ , provided that  $r/H$  also remains constant as an additional parameter. This is only valid when the same grid discretization is used because numerical dispersion was involved in the simulations. Scenarios 3 and 4 had different operational parameters and  $TDS$  concentrations but  $D$ ,  $r/H$ , and the relative durations of the ASR phases were the same for

both scenarios (Table 3). The resulting  $\theta$  and  $RE$  were exactly equal (Appendix 7.2 and 7.5). This confirms that the duration of simulations and experiments can be reduced by doubling the concentrations and the pumping rates (Scenarios 3 and 4). Different combinations of  $K$  and  $n$  were not studied in this research because only one sand type was used.

Although the theory of Bakker (2010) was contradicted, the findings of this study correspond with the study of Ward et al. (2007). He used the mixed convection ratio to characterize ASR systems in brackish aquifers without lateral flow or dispersion. This ratio combines both the  $D$ -parameter of Bakker (2010) and the  $r/H$ -term used in this study. It may thus be a more effective parameter for scaling ASR scenarios in brackish aquifers. However, this was not further examined in this study and further research is required because the mixed convection ratio was not the result of a mathematical derivation (Bakker, 2010).

#### 4.2.2. Influence of aquifer properties and operational parameters on the $RE$ of MPPW-ASR

The conclusions regarding the scalability of conventional ASR systems are also valid for MPPW-ASR, although the ASR performance is different. A lower  $\theta$  resulting from a less significant buoyancy effect (Figure 14 and 15) causes the salinization of the MPPW-ASR well to occur more in the upper part of the aquifer (Appendix 7.8 and 7.9). Consequently, more freshwater is unrecovered and left behind in the lower part of the aquifer, resulting in a decrease in the  $RE$  of MPPW-ASR with a higher  $D$  and a lower  $r/H$  (Figure 13 and 21). On the other hand, a higher  $\theta$  resulting from a more significant buoyancy effect (Figure 14 and 15) causes the salinization of the MPPW-ASR well to occur more at the bottom of the well screen (Appendix 7.8 and 7.9). As a result, more freshwater is unrecovered and left behind in the upper part of the aquifer, which also results in a lower  $RE$  of MPPW-ASR with a lower  $D$  and a higher  $r/H$  (Figure 13 and 20). However, this performance is only valid for the simplified MPPW-ASR operation in this study, including a single partially penetrating extraction well in the upper half of the aquifer with a constant pumping rate. This was not necessarily the optimal operation of MPPW-ASR, as it approximates the behaviour of FPW-ASR when the influence of buoyancy is large. To optimise the  $RE$ , the operation of MPPW-ASR should therefore be adjusted to every specific scenario. The performance of MPPW-ASR is thus not only controlled by the vertical distribution of freshwater in the aquifer, but also by the configuration and operation of the well used, as will become clear from Section 4.5.

#### 4.3. Scaling ASR from a numerical 3D-field setting to the experimental sandbox

The experimental set-up was built to explore and validate the performance of ASR in the representative 3D-field setting, although some discrepancies remain inevitable. This section deals with the second research question, stated as:

*'How can a representative field setting of both conventional ASR and MPPW-ASR effectively be downscaled to the experimental sandbox, and how can the introduced discrepancies be explained?'*

First, the scalability and the discrepancies between the representative numerical 3D-field model and the numerical 2D-field model are discussed in Section 4.3.1. The potential of downscaling the 2D-field model to the 2D-lab model is assessed in Section 4.3.2. The discrepancies introduced by using individual filter screens for an ASR-well instead of a planar well are discussed in Section 4.3.3. Lastly, Section 4.3.4 deals with the differences between physical modelling and numerical modelling.

##### 4.3.1. Scaling ASR between the numerical 3D- and 2D-field settings

The advective displacement of the fresh-salt interface resulting from constant pumping rates is constant in a 2D-setting, whereas it decreases with time in a 3D-setting. The resulting freshwater distribution is also different for both systems (Section 2.7.2). These factors contributed to the discrepancy in the recovered water quality in both settings.

$\theta$  was similar for the 3D-field and 2D-field models for an  $r/H$  of 0.364 (Figure 14 and 15), resulting in a higher  $z_{cm}$  in the former compared to the latter (Figure 16). This led to very different trends in the mixing fraction and the  $RE$  (Figure 18 and 20; Appendix 7.5). The decrease of the  $RE$  of MPPW-ASR with a lower  $D$  (Figure 20) was more significant in the 3D-field model compared to the 2D-field model because more freshwater was left behind in the upper part of the aquifer (Appendix 7.8 and 7.9). The  $RE$  of MPPW-ASR in the 2D-field model is therefore also expected to decrease more significantly with a lower  $D$ , resulting in a higher  $\theta$ . Because  $\theta$  was lower in the 3D-field model compared to the 2D-field model for an  $r/H$  of 0.242 (Figure 14 and 15), the values of  $z_{cm}$  were more alike (Figure 17). As a result, the discrepancy between the  $RE$  in both settings was smaller for both FPW-ASR and MPPW-ASR with an  $r/H$  of 0.242 compared to an  $r/H$  of 0.364 (Figure 18 - 21).

The shape of the freshwater body and the mixing fraction in both 2D- and 3D-models are not simultaneously and consistently scalable to one another solely with the use of  $D$  and  $r/H$  due to the difference in nature of both settings.  $D$  was originally introduced by Bakker (2010) for radial flow and not for 2D flow. Attempts to scale from a 3D-setting to a 2D-setting with alternative scaling parameters, like the mixed convection ratio of Ward et al. (2007) and the storage tilt ratio of Ward et al. (2009), were also unsuccessful. In addition, it was attempted to convert a constant pumping rate for a linear well in a 3D-setting to a decreasing infiltration rate for a planar well in a 2D-setting, such that the movement of the fresh-salt interface would correspond with time. However, it is impossible to simultaneously convert the hydraulic head distribution resulting from pumping in both settings with constant aquifer properties. An alternative but more sophisticated procedure to determine the potential of transferring results from 3D- to 2D-settings is to keep track of the centre of mass of freshwater during ASR, like the method implemented by Van Lopik et al. (2016).

#### 4.3.2. Downscaling ASR from a numerical 2D-field setting to a numerical 2D-lab setting

Also for 2D-settings with a vertical planar well, ASR scenarios with different operational parameters in aquifers with different properties can result in the same  $RE$ , provided that  $D$ ,  $r/H$ , and the relative durations of the ASR phases are constant. This was illustrated by the equal results of the 2D-field model and the 2D-lab model (Appendix 7.2 and 7.5). The  $RE$  was only slightly different as a result of interpolation inaccuracy. This confirms that numerical field-settings of ASR systems with a vertical planar well can effectively be downscaled to a lab-setting, provided that the same grid discretization is used when numerical dispersion is involved.

#### 4.3.3. Discrepancies introduced by the well configuration

The use of multiple filters to simulate ASR in the 2D-filter model was only an approximation of the vertical planar well used in the 2D-lab model. Discrepancies between the results of these models can therefore be fully attributed to the implemented well configuration.

#### Extent of the freshwater body

The individual filter screens were only situated at the front and the rear of the sandbox and had a diameter five times larger than the diameter of the vertical planar well used in the 2D-lab model (Figure 6). Consequently, the extent of the freshwater body was larger at the front and rear walls in the 2D-filter model compared to the 2D-lab model at the initial stages of infiltration (Figure 23 and 24). Furthermore, due to the rough interface between the injected freshwater and ambient saltwater, it was relatively hard and arbitrary to determine  $r_{top}$  and  $r_{bottom}$  in the 2D-filter model. Nevertheless,  $\theta$  of the 2D-filter model approximated that of the 2D-lab model very well after infiltration (Figure 25), and even better after storage (Figure 26) because more time was available for the discrepancies to average out.

### *Increased mixing*

The 2D-filter model was able to reproduce the trends in the *RE* of both FPW-ASR and MPPW-ASR observed in the 2D-lab model (Figure 27 – 31) because of the approximately equal vertical distribution of freshwater in the aquifer. However, the infiltration fronts originating from the individual filter screens were neither connected in the vertical direction, nor in the width dimension at the initial stages of infiltration (Figure 24). Consequently, the total interfacial area between freshwater and ambient saltwater was larger compared to the situation with a vertical planar well (Figure 23). This led to increased mixing of freshwater with ambient saltwater situated in between the individual filter screens, resulting in a more gradual transition of the mixing fraction and a lower *RE* in the 2D-filter model compared to the 2D-lab model (Figure 10, 27 – 30). The individual filter screens thus potentially offer a better correspondence with infiltration and recovery from a vertical planar well that is situated in an aquifer with a higher dispersivity. For MPPW-ASR, the placement of the extraction well 1 cm from the middle of the sandbox also contributed to an earlier extraction of ambient saltwater and to the lower *RE* in the 2D-filter model compared to the 2D-lab model (Figure 6, 29 and 30).

#### *4.3.4. Discrepancies between the physical and numerical lab-scale models*

Numerical modelling can not fully represent the experimental approach. The observed discrepancies between the experiments and the 2D-filter model, including the higher experimental *RE* of FPW-ASR, may be the result of a combination of several factors.

### *Measurement inaccuracies*

The numerical models were an idealization of reality by assuming constant and uniform parameters. However, the experimental infiltration volume had an accuracy of  $\pm 2.5\%$  and the applied pumping rates fluctuated at a maximum degree of  $\pm 10\%$  because they were measured indirectly. The *TDS* concentration in the recovered water was subjected to inaccuracies as well, because it was indirectly computed from the *EC* measurements. In addition, the fresh-salt interface was determined with an accuracy of  $\pm 0.5$  cm. As temperature variations were limited during infiltration and extraction ( $19.5 \pm 1^\circ\text{C}$ ), the effect on density and viscosity was neglected (Ma & Zheng, 2010). However, Van Dooren (2015) showed that these subtle temperature fluctuations can already result in a variation of *K*. Consequently, *K* slightly fluctuated during the experiments and might have differed from that documented by Van Dooren (2015). These inaccuracies also limit the reproducibility of the experimental results themselves.

### *Heterogeneities*

Packing the sand with the method of Rietdijk et al. (2010) was assumed to result in the same uniform *K* and *n* as documented by Van Dooren (2015). However, the presence of the ASR-well in the experiments complicated the packing procedure, which might have introduced slight heterogeneities and preferential flow paths close to the well. Additionally, the packing of sand close to the glass walls was affected by the presence of the wall, as the permeability increased relative to that of the main body of the medium (Simmons et al., 2002). The ratio between the  $d_{50}$  of the sand and the medium's diameter should be lower than 0.025 to ensure that flow parameters are independent of such wall effects (Fand & Thinakaran, 1990). The ratio in this study equalled 0.004, indicating that wall effects were negligible for the average flow patterns. However, the movement of tracer dye at the wall may be affected, thereby overestimating the visible movement of the freshwater body.

### *Unequal distribution of infiltration rates*

The infiltration rate was assumed to be equally distributed over all individual filter screens in the experimental set-up. However, more freshwater appeared to be infiltrated via the upper filter screens compared to the lower ones, even for the situation with a negligible density

difference (*Appendix 7.6*). A decreased degree of packing in the upper part of the aquifer might have introduced preferential flowpaths, contributing to the easier infiltration through the upper filter screens. Moreover, Petersen et al. (1955), referred to by Houben (2015), stated that in long well screens situated in actual porous media, only the upper part may contribute significantly to the total inflow. Houben (2015) also stated that the strongest inflow peak occurs at the top of the well when the pump is installed above the well screen. These effects may have contributed to the higher  $\theta$  in the experiments compared to that in the 2D-filter model (*Figure 32 and 33*). Similar preferential flowpaths probably existed during extraction because the mixing fraction of the experiments approximated that of the 2D-filter model generally well (*Appendix 7.5*).

#### *Dispersivity*

The ASR performance in the experimental set-up is not only controlled by  $D$ ,  $r/H$ , and the relative durations of the ASR phases. It is also controlled by the experimental dispersivity (Ward et al., 2009; Barker et al., 2016). On the other hand, the experiments do not include numerical dispersion. The exact effect of both types of dispersion and their relationship were, however, not further examined in this study and thus their invalid fitting procedure contributes to the discrepancy between physical and numerical modelling.

#### *4.4. Improved recovery efficiency (RE) of MPPW-ASR compared to FPW-ASR*

The results of  $\Delta RE$  and  $\%RE$  were used to examine the third research question, stated as: 'What is the improvement in the RE of MPPW-ASR compared to FPW-ASR for different situations in a representative field setting and in the experimental sandbox?'

The improved RE of MPPW-ASR compared to FPW-ASR for the representative numerical 3D-field setting is discussed in *Section 4.4.1*. The representativeness of the experimental sandbox is assessed in *Section 4.4.2*, which also allows to address the main hypothesis of this research.

##### *4.4.1. Improved RE of MPPW-ASR compared to FPW-ASR in the representative field setting*

The positive values of  $\%RE$  and  $\Delta RE$  indicate that MPPW-ASR was indeed more efficient than FPW-ASR for most situations in the 3D-field model (*Figure 22, 39 and 40*). However, the decrease of the added value of MPPW-ASR over FPW-ASR with a higher  $D$  and a lower  $r/H$  was mainly caused by the increasing RE of FPW-ASR with less influence of buoyancy (*Figure 12 and 19*). The related decrease of the RE of MPPW-ASR was less significant (*Figure 13 and 21*). The negative  $\%RE$  and  $\Delta RE$  for situations with a negligible buoyancy effect can be attributed to the simplified MPPW-ASR operation in this study, as will be further discussed in *Section 4.5*. The simplified operation of MPPW-ASR also caused the  $\Delta RE$  to decrease with a more significant buoyancy effect in the 3D-field model, due to the decrease of the RE of MPPW-ASR (*Figure 20*). This trend was not evident from the  $\%RE$ , since FPW-ASR resulted in a negligible RE. Although the  $\%RE$  ranged between -4%, for a  $D$  of 2.393 and an  $r/H$  of 0.242, and 1434%, for a  $D$  of 0.957 and an  $r/H$  of 0.364, in the 3D-field model, this quantification strongly depends on the configuration and operation of the well screen.

The increase of the RE of FPW-ASR with a higher  $D$  and a lower  $r/H$  was also evident from the 2D-field model. However, the  $\%RE$  ranged between -8% and 280%, indicating that the use of a vertical planar well resulted in an underestimation of the improved RE that can be achieved by using a linear well. Nevertheless, the results of both models are not consistently transferable because of the difference in nature between 2D- and 3D- settings (*Section 4.3.1*).

##### *4.4.2. Representativeness of the experimental sandbox*

The experiments do not represent a down-scaled version of an ASR-setting in the field with a vertical linear well. However, the experimental set-up is generally suitable for representing 2D-settings of ASR including a vertical planar well. The general morphology of the



freshwater body and the flow patterns observed in the numerical 2D-field model were reproduced in the experimental set-up. The increase of the  $RE$  of FPW-ASR with a higher  $D$  and a lower  $r/H$  was also evident from the experimental results, just as the resulting decrease of  $\Delta RE$  and  $\%RE$ . Additionally, the sandbox is more suitable for experimenting with a more significant buoyancy effect or with longer durations of infiltration. For such scenarios, the influence of buoyancy overshadows the experimental limitations and the errors introduced by the well configuration in the middle of the domain. Therefore, the experimental sandbox is a valuable validation and visualisation tool for 2D-settings of ASR with a vertical planar well in brackish aquifers. Accordingly, the validation part of the main hypothesis is accepted.

However, the quantification part of the main hypothesis is rejected. The  $\%RE$  ranged between -21% and 192% in the 2D-filter model, indicating that the increased mixing resulting from the individual filter screens resulted in an underestimation of the improved  $RE$  that can be achieved by using a vertical planar ASR well. The experimental  $\%RE$  ranged between -33% and 102%, indicating that the discrepancies between physical and numerical modelling cause the numerical 2D-filter model to overestimate the improved  $RE$  observed in the experiments. Thus, the experimental sandbox can not be used as a quantification tool for determination of the exact  $RE$  of ASR in brackish aquifers.

Considering the limitations of both numerical simulations and sandbox experiments, it is hard to state which approach better represents an actual field setting of ASR. The combination of physical and numerical modelling is especially valuable for predicting and visualising field applications.

#### 4.5. Implications for practical application

The controlling parameters for ASR in the field and the optimisation of MPPW-ASR were considered in this section in order to answer the fourth research question, stated as: 'What are the implications of the results for the practical application?'

##### *4.5.1. Additional controlling parameters for ASR in the field*

This study suggested that FPW-ASR is not only less efficient with a lower  $D$  (Bakker, 2010), but also with a longer duration of infiltration (a higher  $r/H$ ), both contributing to a more significant buoyancy effect. Mixing by dispersion can also reduce the  $RE$  of ASR (Ward et al., 2009; Barker et al., 2016). On top of this, aquifer heterogeneity, lateral groundwater flow, and geochemical interactions with the aquifer matrix may all negatively affect the  $RE$  of ASR in the field (Moulder, 1970; Maliva et al., 2006; Ward et al., 2008; Bakker, 2010; Zuurbier et al., 2013; 2016a; Guo et al., 2015). The aquifer in this research was bounded by an impermeable base and a confining bentonite clay layer. However, the target aquifer in the Westland area of the Netherlands is actually bounded by two aquitards with a  $K$  of 0.05 – 1 m d<sup>-1</sup> (e.g. Ros & Zuurbier, 2016; Zuurbier & Stuyfzand, 2016). As a result, the interaction with the bounding aquitards was not comparable with that specific field setting, potentially resulting in an overestimation of the  $RE$ .

The range of pumping rates (200 – 500 m<sup>3</sup> d<sup>-1</sup>) used in the numerical 3D-field model for a TDS concentration of 8.7 g L<sup>-1</sup> was comparable to actual ASR applications in the Westland area (Zuurbier & Stuyfzand, 2016). However, pumping rates are usually adjusted to the freshwater surplus and demand and may vary over time. Moreover, the scenarios studied in this research corresponded with short-term (1 – 7 days of infiltration) ASR applications in the field with a relatively small infiltration volume (952 – 2142 m<sup>3</sup>) (Table 1). This was not representative for the typical seasonal pattern of precipitation surplus and freshwater demand for greenhouse horticulture in the Westland area (Zuurbier et al., 2013; Zuurbier & Stuyfzand, 2016). In addition, the recovery phase of ASR will be terminated either when a certain threshold concentration is exceeded, or when the water demand is met. The duration of storage also depends on the timing of the freshwater demand. As a result, predictive

simulations and lab-experiments for ASR in the field are restricted by the uncertainty of the size and timing of the freshwater surplus and demand. Nevertheless, the larger added value of MPPW-ASR compared to FPW-ASR with a larger influence of buoyancy is also expected to be valid in the field, since the dimensionless parameters used in this study can be transferred to any scale or scenario with the limitations described before kept in mind.

Lastly, it is rather arbitrary to use the  $RE$  for a mixing fraction threshold of 0.9. It necessarily introduces the corresponding limiting recoverable concentration as another variable to influence the results (Ward et al., 2007). However, similar trends were observed for an  $RE$  corresponding with a mixing fraction of 0.95, thereby not impacting the observed increase in  $\%RE$  with a larger influence of buoyancy.

#### 4.5.2. *Optimisation of MPPW-ASR*

The focus of this research was on validating rather than optimising the increased  $RE$  of MPPW-ASR compared to FPW-ASR. Extraction by a single MPPW-ASR well in the upper half of the aquifer was perhaps not the optimal application, but was rather a simplification limited by the well used in the physical sandbox of this research. The fact that MPPW-ASR with such a static well already resulted in a higher  $RE$  than FPW-ASR for most situations, indicates that there is definitely a benefit in replacing conventional fully penetrating wells by more dedicated well configurations for ASR systems in coastal aquifers.

The installation of multiple filter screens at different depths would be a more dedicated application of MPPW-ASR by increasing the vertical control of freshwater injection and recovery (Zuurbier et al., 2014). In such cases, the most suitable operation of infiltration and recovery can be chosen for the aquifer in question. Extraction from one filter screen can for example be terminated when a threshold concentration is met, and another filter screen can be selected for the best quality of recovered water. Because the aim of MPPW-ASR is to counteract the negative effect of buoyancy on the  $RE$ , the most optimal application of MPPW-ASR is independent of  $D$  and  $r/H$ . Such an application would ameliorate the decreased  $\Delta RE$  for the very low  $D$  and high  $r/H$  and the negative  $\Delta RE$  and  $\%RE$  at a high  $D$  and a low  $r/H$  observed in this study. As a result, MPPW-ASR can always be at least as efficient as FPW-ASR in brackish aquifers, as long as it is implemented in the most suitable way for a given scenario. However, the added value of MPPW-ASR over FPW-ASR will always decrease with a less significant buoyancy effect, because the  $RE$  of FPW-ASR increases for such situations. In addition, the significance of the improved  $RE$  is expected to decrease at every step the well configuration and operation become more sophisticated.

Thus, multiple partially penetrating wells are valuable for increasing the  $RE$  of ASR, especially when there is a large concentration gradient between infiltrated freshwater and ambient saltwater. Consequently, the variation of the freshwater surplus and demand in coastal areas can be balanced more efficiently. This reduces the stress on freshwater resources and increases the sustainability of freshwater management in coastal areas.

#### 4.6. *Recommendations*

When higher  $D$ -values have to be studied in the existing experimental set-up, one is advised to lower the concentration contrast instead of increasing the pumping rate. At higher pumping rates than studied in this research, the infiltration pressure increases and the bentonite clay layer may separate from the sand, thereby disturbing the packing of the aquifer and affecting the results by introducing preferential flow paths. Experimenting with a lower  $D$  and a higher  $r/H$  was limited in this study by the proximity of the constant head reservoirs. In future experiments, the thickness of the aquifer can, however, be reduced. In that case, the performance of the ASR-construction should first be assessed, as the relative vertical distribution of the individual filter screens changes.

More dedicated well configurations for MPPW-ASR might be developed in future experimental studies to validate the results of Zuurbier et al. (2014) even further. The experimental set-

up may also be useful to validate the results of Zuurbier et al. (2016) regarding the improved  $RE$  of HDDW-ASR compared to FPW-ASR. The bentonite layer can be removed to study the implementation of ASR in unconfined aquifers. Furthermore, a more realistic construction can be developed to represent a planar well that introduces less mixing compared to the individual filter screens. Alternatively, the length of the sandbox and the infiltration volume can be increased to reduce the effect of the applied well-configuration in the middle of the aquifer.

In future research, the  $R_{disp}$  parameter of Ward et al. (2009) and Barker et al. (2016) could be used to correctly scale dispersion effects. The centre of mass (Van Lopik et al., 2016) can be used as a parameter to effectively determine the discrepancy and scalability between 2D- and 3D-settings with regard to the mixing fraction, and to improve the representativeness of the sandbox. Alternatively, future research can be focused on performing experiments with a physical model that better approximates an axi-symmetric field situation. A suggestion is to experiment with a physical model shaped as a circular sector ('pizza slice') with the well placed in the tip. Model simulations might then be performed with 2D axi-symmetric models, of which the potential has already been demonstrated (e.g. Langevin & Zygnerski, 2006; Ward et al, 2008; Zuurbier et al., 2014).



## 5. Conclusions

The unviability of conventional ASR with a larger influence of buoyancy (a lower  $D$ ) was confirmed in this study with a representative 3D-field scale model. For a given  $D$ , the  $RE$  was also lower with a longer duration of infiltration (a higher  $r/H$ ), because there was more time for the fresh-salt interface to tilt. This contradicts the findings of Bakker (2010), who stated that the  $RE$  of ASR is only controlled by  $D$  and by the relative durations of the ASR phases. This could be due to the difference in the definition of  $RE$ , to numerical dispersion, or to the invalidity of the solution of Bakker (2010) for low  $D$  values.

Nevertheless, the  $RE$  of ASR scenarios with different aquifer properties and operational parameters can be equal, provided that  $D$ ,  $r/H$  and the relative lengths of the ASR phases are constant. This enables downscaling of ASR systems from a field-setting to a lab-setting. In numerical models, the grid discretization should also be equal if numerical dispersion is involved. In physical models, the  $RE$  of ASR is also controlled by the experimental dispersion. In the field, additional properties like aquifer heterogeneity and lateral groundwater flow also determine the  $RE$  of ASR. Numerical modelling is thus an idealization of reality but can provide useful insights for practical applications.

MPPW-ASR was simulated by infiltration over the complete aquifer thickness but by extraction with a single partially penetrating well in the upper half of the aquifer. For this MPPW-ASR operation, the  $RE$  generally improved compared to FPW-ASR. However, the absolute and relative improvements ( $\Delta RE$  and  $\%RE$ ) decreased with a less significant buoyancy effect (a lower  $r/H$  and a higher  $D$ ) and were even negative for a very high  $D$  and a low  $r/H$ . For a very large influence of buoyancy, the simplified MPPW-ASR operation approximated the behaviour of FPW-ASR, eventually resulting in a poor recovery potential.

If the operation of MPPW-ASR would be more sophisticated, the  $RE$  of MPPW-ASR could always be ameliorated compared to that of FPW-ASR in brackish aquifers. The beneficial effect of MPPW-ASR thus lies mostly in its flexibility, although most of the improvement might already have been covered with the simplified MPPW-ASR operation in this study. The added value of MPPW-ASR definitely decreases with a lower  $r/H$  and a higher  $D$ , because the  $RE$  of FPW-ASR increases with a less significant buoyancy effect.

The shape of the freshwater body and the  $RE$  in a 3D-setting with a vertical linear well were not simultaneously transferrable to a 2D-setting with a vertical planar well when solely  $D$  and  $r/H$  were used for scaling. This is due to the different nature of both settings. Future studies are advised to use alternative parameters for scaling or to use a different experimental set-up.

Considering the main hypothesis, the 2D lab-scale sandbox model was able to visualise the flow patterns and to validate the added value of MPPW-ASR over FPW-ASR observed in the numerical 2D-settings with a vertical planar well. The decrease of the added value with a higher  $D$  and a lower  $r/H$  was also validated. However, the experimental results underestimated the improvement in the  $RE$  that was achieved in the numerical field-scale models. This was mostly due to increased mixing as a result of the experimental well configuration and (numerical) dispersion. Moreover, the experiments were not representative for a 3D-setting with a vertical linear well. In conclusion, the experimental sandbox should mainly be considered as a validation and visualisation tool and not as a quantification tool for ASR systems in brackish aquifers.



## 6. References

- Abarca, E., & Clement, T. P. (2009). A novel approach for characterizing the mixing zone of a saltwater wedge. *Geophysical research letters*, 36, L06402.
- Bakker, M. (2010). Radial Dupuit interface flow to assess the aquifer storage and recovery potential of saltwater aquifers. *Hydrogeology Journal*, 18(1), 107-115.
- Barker, J. L., Hassan, M. M., Sultana, S., Ahmed, K. M., & Robinson, C. E. (2016). Numerical evaluation of community-scale aquifer storage, transfer and recovery technology: A case study from coastal Bangladesh. *Journal of Hydrology*, 540, 861-872.
- Beyer, W. (1987). *CRC Standard Mathematical Tables, 28th edition*. Boca Raton, FL: CRC Press.
- Chiang, E. W. (2012). *Processing modflow: An integrated modeling environment for the simulation of groundwater flow, transport and reactive processes, in 8.06 ed*. Irvine, USA: Simcore Software.
- Esmail, O. J., & Kimbler, O. K. (1967). Investigation of the technical feasibility of storing fresh water in saline aquifers. *Water Resources Research*, 3(3), 683-695.
- Fand, R. M., & Thinakaran, R. (1990). The influence of the wall on flow through pipes packed with spheres. *Journal of Fluids engineering*, 112(1), 84-88.
- Fitts, C. (2002). *Groundwater Science*. Waltham, USA: Elsevier Inc. Academic Press.
- Goswami, R. R., & Clement, T. P. (2007). Laboratory-scale investigation of saltwater intrusion dynamics. *Water Resources Research*, 43(4), W04418.
- Guo, W., & Langevin, C. (2002). *User's guide to SEAWAT; a computer program for simulation of three-dimensional variable-density ground-water flow*. Tallahassee, Florida, USA: U.S. Geological Survey.
- Guo, W., Coulibaly, K., & Maliva, R. G. (2015). Simulated effects of aquifer heterogeneity on ASR system performance. *Environmental Earth Sciences*, 73(12), 7803-7809.
- Harris, J. W., & Stöcker, H. (1998). Trapezoid §3.6.2. In *Handbook of mathematics and computational science* (pp. 82-83). New York: Springer-Verslag New York, Inc.
- Herrera, P., & Valocchi, A. (2006). Positive Solution of Two-Dimensional Solute Transport in Heterogeneous Aquifers. *Ground water*, 44(6), 803-813.
- Houben, G. J. (2015). Review: Hydraulics of water wells—flow laws and influence of geometry. . *Hydrogeology Journal*, 23(8), 1633-1657.
- Langevin, C. D., & Zygnerski, M. (2006). Axisymmetric simulation of aquifer storage and recovery with SEAWAT and the Sea Water Intrusion (SWI) Package for MODFLOW. *Proceedings of MODFLOW and More 2006, Managing Ground-Water System*, 465-469.
- Langevin, C., Thorne, D., Dausman, A., Sukop, M., & Guo, W. (2008). *SEAWAT Version 4: A Computer Program for Simulation of Multi-Species Solute and Heat Transport*. Reston, Virginia, USA: U.S. Geological Survey.
- Luyun, R. J., Momii, K., & Nakagawa, K. (2011). Effects of Recharge Wells and Flow Barriers on Seawater Intrusion. *Ground Water*, 49(2), 239-249.
- Ma, R., & Zheng, C. (2010). Effects of Density and Viscosity in Modeling Heat as a Groundwater Tracer. *Ground Water*, 48 (3), 380-389.

- Maliva, R. G., Guo, W., & Missimer, T. M. (2006). Aquifer storage and recovery: recent hydrogeological advances and system performance. *Water environment research*, 78(13), 2428-2435.
- Marton Geotechnical Services Ltd. (2015). *Bentonite Pellets - Mikolit*. (n.d.). Retrieved from MGS: <http://www.mgs.co.uk/boreholes/borehole-sealing/118/bentonite-pellets---mikolit.html>
- Merritt, M. L. (1986). Recovering fresh water stored in saline limestone aquifers. *GROUND WATER*, 24(4), 516-529.
- Missimer, T., Guo, W., Walker, C., & Maliva, R. (2002). Hydraulic and density considerations in the design of aquifer storage and recovery systems. *Florida Water Resources Journal*, 55(2), 30-36.
- Moulder, E. (1970). Freshwater bubbles: a possibility for using saline aquifers to store water. *Water Resources research*, 6(5), 1528-1531.
- Pavelic, P., Dillon, P., & Simmons, C. (2002). Lumped parameter estimation of initial recovery efficiency during aquifer storage and recovery. *Management of Aquifer Recharge for Sustainability, Proceedings of the fourth International Symposium on Artificial Recharge (ISAR4), Adelaide*, 285–290.
- Pennink, J. (1915). *Grondwater Stroombanen*. Amsterdam: Stadsdrukkery.
- Petersen, J. S., Rohwer, C., & Albertson, M. L. (1955). Effect of well screen on flow into wells. *Transactions of the American Society of Civil Engineers*, 120(1), 563–585.
- Pyne, R. (2005). *Aquifer Storage Recovery - A guide to Groundwater Recharge Through Wells*. Gainesville, Florida, USA: ASR Systems LLC.
- Rietdijk, J., Schenkeveld, F., Schaminée, P., & Bezuijen, A. (2010). The drizzle method for sand sample preparation. *Proceedings of the International Conference on Physical Modelling in Geotechnics (ICPMG), 1*, 267-272.
- Robinson, G., Ahmed, A. A., & Hamill, G. (2016). Experimental saltwater intrusion in coastal aquifers using automated image analysis: Applications to homogeneous aquifers. *Journal of Hydrology*, 538, 304-313.
- Ros, S., & Zuurbier, K. G. (2016). *The effects of large-scale implementation of ASRO on the fresh-salt water distribution in the Westland groundwater system*. Nieuwegein, The Netherlands: DESSIN & KWR Watercycle Research Institute .
- Schäfer, W. (2016). *Applied 3-D Groundwater Modeling with MODFLOW/MT3D/MT3DMS - Transport Modeling*. Retrieved from Dr.-Ing. Wolfgang Schäfer: Grundwassermodellierung: [http://www.schaefer-gwm.de/downloads/transport\\_modeling.pdf](http://www.schaefer-gwm.de/downloads/transport_modeling.pdf)
- Simmons, C., Pierini, M., & Hutson, J. (2002). Laboratory Investigation of Variable-Density Flow and Solute Transport in Unsaturated-Saturated Porous Media. *Transport in Porous Media*, 47, 215-244.
- Small, C., & Nicholls, R. J. (2003). A Global Analysis of Human Settlement in Coastal Zones. *Journal of Coastal Research*, 19(3), 584-599.
- Stoeckl, L., & Houben, G. (2012). Flow dynamics and age stratification of freshwater lenses. *Journal of Hydrology*, 458-459(0), 9-15.
- Svendsen, I. A. (1985). Physical modelling of water waves. *Physical Modelling in Coastal Engineering*. AA Balkema, Rotterdam, 13-48.



- Van Dooren, T. C. (2015). *Investigation of various sand column preparation procedures for non-Darcy groundwater flow experiments*. Utrecht, The Netherlands: Unpublished bachelor's thesis, Utrecht University.
- Van Ginkel, M., Des Tombe, B., Olsthoorn, T., & Bakker, M. (2016). Small-Scale ASR Between Flow Barriers in a Saline Aquifer. *Groundwater*, 1-11.
- Van Ginkel, M., Olsthoorn, T., & Bakker, M. (2014). A New Operational Paradigm for Small-Scale ASR in Saline Aquifers. *Groundwater*, 52(5), 685-693.
- van Lopik, J., Hartog, N., Zaadnoordijk, W., Cirkel, D., & Raoof, A. (2016). Salinization in a stratified aquifer induced by heat transfer from well casings. *Advances in Water Resources*, 86, 32 - 45.
- Vörösmarty, C. J., Green, P., Salisbury, J., & Lammers, R. B. (2000). Global Water Resources: Vulnerability from Climate Change and Population Growth. *Science*, 289(5477), 284-288.
- Ward, J. D., Simmons, C. T., Dillon, P. J., & Pavelic, P. (2009). Integrated assessment of lateral flow, density effects and dispersion in aquifer storage and recovery. *Journal of Hydrology*, 370 (1-4), 83-99.
- Ward, J., Simmons, C., & Dillon, P. (2007). A theoretical analysis of mixed convection in aquifer storage and recovery: How important are density effects? *Journal of Hydrology*, 343(3-4), 169-186.
- Ward, J., Simmons, C., & Dillon, P. (2008). Variable-density modelling of multiple-cycle aquifer storage and recovery (ASR): Importance of anisotropy and layered heterogeneity in brackish aquifers. *Journal of Hydrology*, 356(1-2), 93-105.
- Werner, A. D., Jakovovic, D., & Simmons, C. T. (2009). Experimental observations of saltwater up-coning. *Journal of Hydrology*, 373, 230-241.
- Zhao, J., WenZhong, H., ShuLong, C., Zhen, L., ZhouCong, Z., & LiuLi, H. (2009). A Laboratory Model of the Evolution of an Island Freshwater Lens. *IAHS Press, Hyderabad*, 154-161.
- Zheng, C., & Bennett, G. D. (2002). *Applied Contaminant Transport Modelling*. New York, USA: Wiley Interscience: John Wiley & Sons, Inc.
- Zheng, C., & Wang, P. P. (1999). *MT3DMS: a modular three-dimensional multispecies transport model for simulation of advection, dispersion, and chemical reactions of contaminants in groundwater systems; documentation and user's guide*. Tuscaloosa, AL, USA: University of Alabama.
- Zuurbier, K. G., & Paalman, M. (2014). *Veldproef ondergrondse zoetwaterberging in zout grondwater (Pilot ASR Prominent)*. KvK 115/2014: Nationaal Onderzoeksprogramma Kennis voor Klimaat.
- Zuurbier, K. G., Raat, K. J., Paalman, M., Oosterhof, A. T., & Stuyfzand, P. J. (2016b). How Subsurface Water Technologies (SWT) can Provide Robust, Effective, and Cost-Efficient Solutions for Freshwater Management in Coastal Zones. *Water Resources Management*, 1-17.
- Zuurbier, K., & Stuyfzand, P. (2016). Consequences and mitigation of saltwater intrusion induced by short-circuiting during aquifer storage and recovery (ASR) in a coastal, semi-confined aquifer (submitted for publication). *Hydrology and Earth System Sciences*, 1-26.
- Zuurbier, K., Bakker, M., Zaadnoordijk, W., & Stuyfzand, P. (2013). Identification of potential sites for aquifer storage and recovery (ASR) in coastal areas using ASR performance estimation methods. *Hydrogeology Journal* 21(6), 1373-1383.

- Zuurbier, K., Hartog, N., & Stuyfzand, P. (2016a). Reactive transport impacts on recovered freshwater quality for a field MPPW-ASR system in a brackish and geochemically heterogeneous coastal aquifer. *Applied Geochemistry*, 71, 35-47.
- Zuurbier, K., Kooiman, J., Groen, M., Maas, B., & Stuyfzand, P. (2015). Enabling Successful Aquifer Storage and Recovery of Freshwater Using Horizontal Directional Drilled Wells in Coastal Aquifers. *Journal of Hydrologic Engineering*, 20(3), B4014003.
- Zuurbier, K., Zaadnoordijk, W., & Stuyfzand, P. (2014). How multiple partially penetrating wells improve the freshwater recovery of coastal aquifer storage and recovery (ASR) systems: A field and modelling study. *Journal of Hydrology*, 509(0), 430-441.

## 7. Appendices

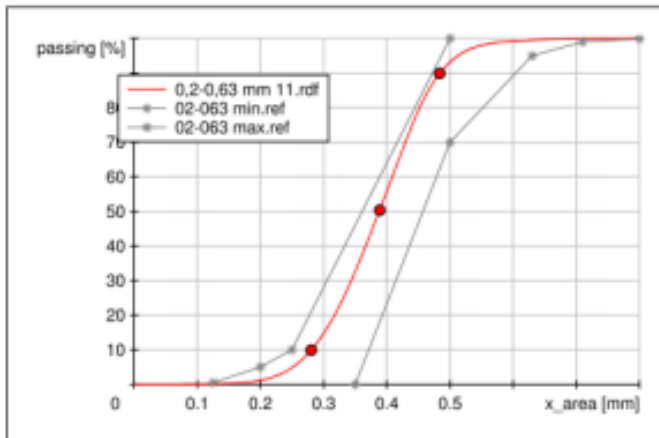
### 7.1. Granulometric data of filtersand used in this research

## Filtersand 0.2-0.63 mm

Technical Data

### GRANULOMETRIC DATA

Size class [mm]	on sieve [%]	passing [% cum.]	retained [% cum.]
0.800 - 1.140	0.0	100.0	0.0
0.710 - 0.800	0.1	100.0	0.0
0.630 - 0.710	0.4	99.9	0.1
0.600 - 0.630	0.3	99.5	0.5
0.500 - 0.600	6.1	99.2	0.8
0.425 - 0.500	25.2	93.1	6.9
0.400 - 0.425	12.2	67.9	32.1
0.355 - 0.400	20.9	55.7	44.3
0.315 - 0.355	15.6	34.8	65.2
0.300 - 0.315	4.5	19.2	80.8
0.250 - 0.300	9.9	14.7	85.3
0.200 - 0.250	3.6	4.8	95.2
0.180 - 0.200	0.6	1.2	98.8
0.150 - 0.180	0.3	0.6	99.4
0.125 - 0.150	0.2	0.3	99.7
0.014 - 0.125	0.1	0.1	99.9
0.000 - 0.014	0.0	0.0	100.0



#### Characteristics

Q3 [%]	x [mm]
95.0	0.513
50.0	0.388
10.0	0.281
x [mm]	1-Q3 [%]
0.630	0.5
0.400	44.3
0.200	98.8
UC =	1.455

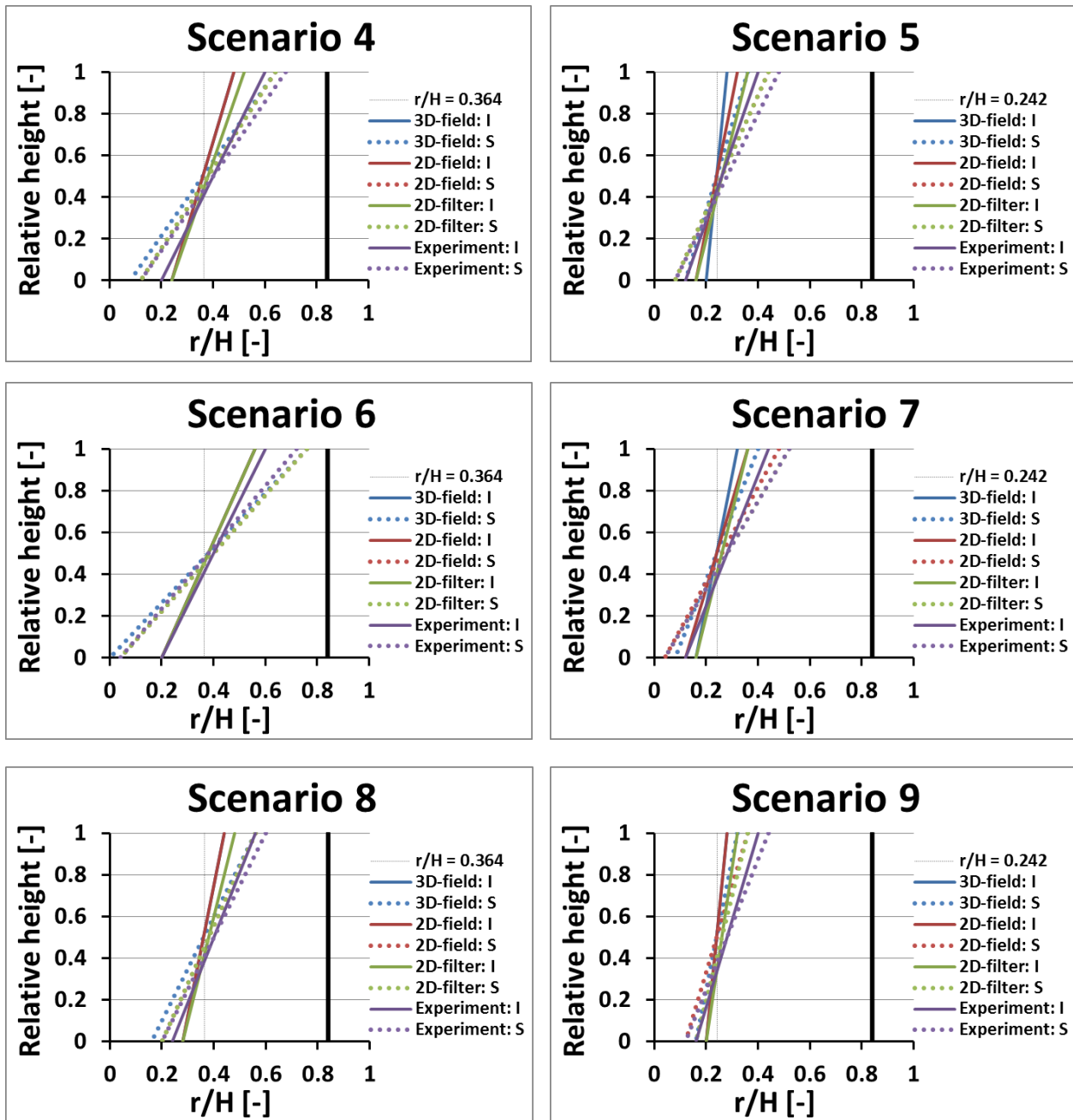
TDS. 2011-Filter sand 0.2-0.63 mm/11 1/2

7.2. Dimensions of the freshwater body and RE for all individual models and scenarios

Scenario 1	Infiltration			Storage			Recovery	
	$r_{top}$	$r_{bottom}$	$\vartheta$	$r_{top}$	$r_{bottom}$	$\Theta$	Wells	RE
Model B	9	9	0	9	9	0	FPW	0.901
Model C	9	9	0	9	9	0	FPW	0.902
Model D	9	9	0	9	9	0	FPW	0.746
Scenario 2	Infiltration			Storage			Recovery	
	$r_{top}$	$r_{bottom}$	$\vartheta$	$r_{top}$	$r_{bottom}$	$\Theta$	Wells	RE
Model C	9	9	0	10	8	0.08	FPW	0.884
Model D	9	9	0	10	9	0.04	FPW	0.733
Model E	13	6	0.28	13	6	0.28	FPW	0.807
Scenario 3	Infiltration			Storage			Recovery	
	$r_{top}$	$r_{bottom}$	$\Theta$	$r_{top}$	$r_{bottom}$	$\Theta$	Wells	RE
Model A	12	6	0.24	16	2	0.56	FPW MPPW	0.088 0.594
Model B	12	6	0.24	16	3	0.52	FPW MPPW	0.387 0.729
Model C	12	6	0.24	16	3	0.52	FPW MPPW	0.387 0.730
Model D	13	6	0.28	16	3	0.52	FPW MPPW	0.357 0.571
Scenario 4	Infiltration			Storage			Recovery	
	$r_{top}$	$r_{bottom}$	$\Theta$	$r_{top}$	$r_{bottom}$	$\vartheta$	Wells	RE
Model A	12	6	0.24	16	2	0.56	FPW MPPW	0.088 0.595
Model B	12	6	0.24	16	3	0.52	FPW MPPW	0.387 0.731
Model C	12	6	0.24	16	3	0.52	FPW MPPW	0.387 0.731
Model D	13	6	0.28	16	3	0.52	FPW MPPW	0.357 0.572
Model E	15	5	0.4	17	3	0.56	FPW MPPW	0.442 0.551
Scenario 5	Infiltration			Storage			Recovery	
	$r_{top}$	$r_{bottom}$	$\Theta$	$r_{top}$	$r_{bottom}$	$\Theta$	Wells	RE
Model A	7	5	0.08	9	3	0.24	FPW MPPW	0.342 0.564
Model B	8	4	0.16	11	2	0.36	FPW MPPW	0.469 0.651
Model C	8	4	0.16	11	2	0.36	FPW MPPW	0.469 0.651
Model D	9	4	0.2	11	2	0.36	FPW MPPW	0.345 0.411
Model E	10 11	3 3	0.28 0.32	12 12	2 2	0.4 0.4	FPW MPPW	0.497 0.438

Scenario 6	Infiltration			Storage			Recovery	
	$r_{top}$	$r_{bottom}$	$\Theta$	$r_{top}$	$r_{bottom}$	$\Theta$	Wells	RE
Model A	14	5	0.36	19	0	0.76	FPW MPPW	0.024 0.368
Model B	14	5	0.36	19	1	0.72	FPW MPPW	0.188 0.714
Model C	14	5	0.36	19	1	0.72	FPW MPPW	0.189 0.714
Model D	14	5	0.36	19	1	0.72	FPW MPPW	0.206 0.601
Model E	15	5	0.4	18	1	0.68	FPW	0.274
	14	5	0.36	17	1	0.64	MPPW	0.553
Scenario 7	Infiltration			Storage			Recovery	
	$r_{top}$	$r_{bottom}$	$\Theta$	$r_{top}$	$r_{bottom}$	$\Theta$	Wells	RE
Model A	8	4	0.16	10	2	0.32	FPW MPPW	0.156 0.566
Model B	9	3	0.24	12	1	0.44	FPW MPPW	0.267 0.670
Model C	9	3	0.24	12	1	0.44	FPW MPPW	0.267 0.671
Model D	9	4	0.2	13	1	0.44	FPW MPPW	0.204 0.441
Model E	11	3	0.32	13	1	0.48	FPW MPPW	0.294 0.422
Scenario 8	Infiltration			Storage			Recovery	
	$r_{top}$	$r_{bottom}$	$\Theta$	$r_{top}$	$r_{bottom}$	$\Theta$	Wells	RE
Model A	11	7	0.16	14	4	0.4	FPW MPPW	0.296 0.660
Model B	11	7	0.16	14	5	0.36	FPW MPPW	0.603 0.704
Model C	11	7	0.16	14	5	0.36	FPW MPPW	0.603 0.704
Model D	12	7	0.2	14	5	0.36	FPW MPPW	0.526 0.540
Model E	14	6	0.32	15	5	0.4	FPW	0.657
	15	6	0.36	16	5	0.44	MPPW	0.590
Scenario 9	Infiltration			Storage			Recovery	
	$r_{top}$	$r_{bottom}$	$\Theta$	$r_{top}$	$r_{bottom}$	$\Theta$	Wells	RE
Model A	7	5	0.08	8	4	0.16	FPW MPPW	0.563 0.544
Model B	7	5	0.08	9	3	0.24	FPW MPPW	0.664 0.617
Model C	7	5	0.08	9	3	0.24	FPW MPPW	0.660 0.614
Model D	8	5	0.12	9	4	0.2	FPW MPPW	0.471 0.374
Model E	10	4	0.24	11	3	0.32	FPW MPPW	0.660 0.448

7.3. Slope and position of the fresh-salt interface after infiltration (I) and storage (S) in all models for scenarios 4 – 9

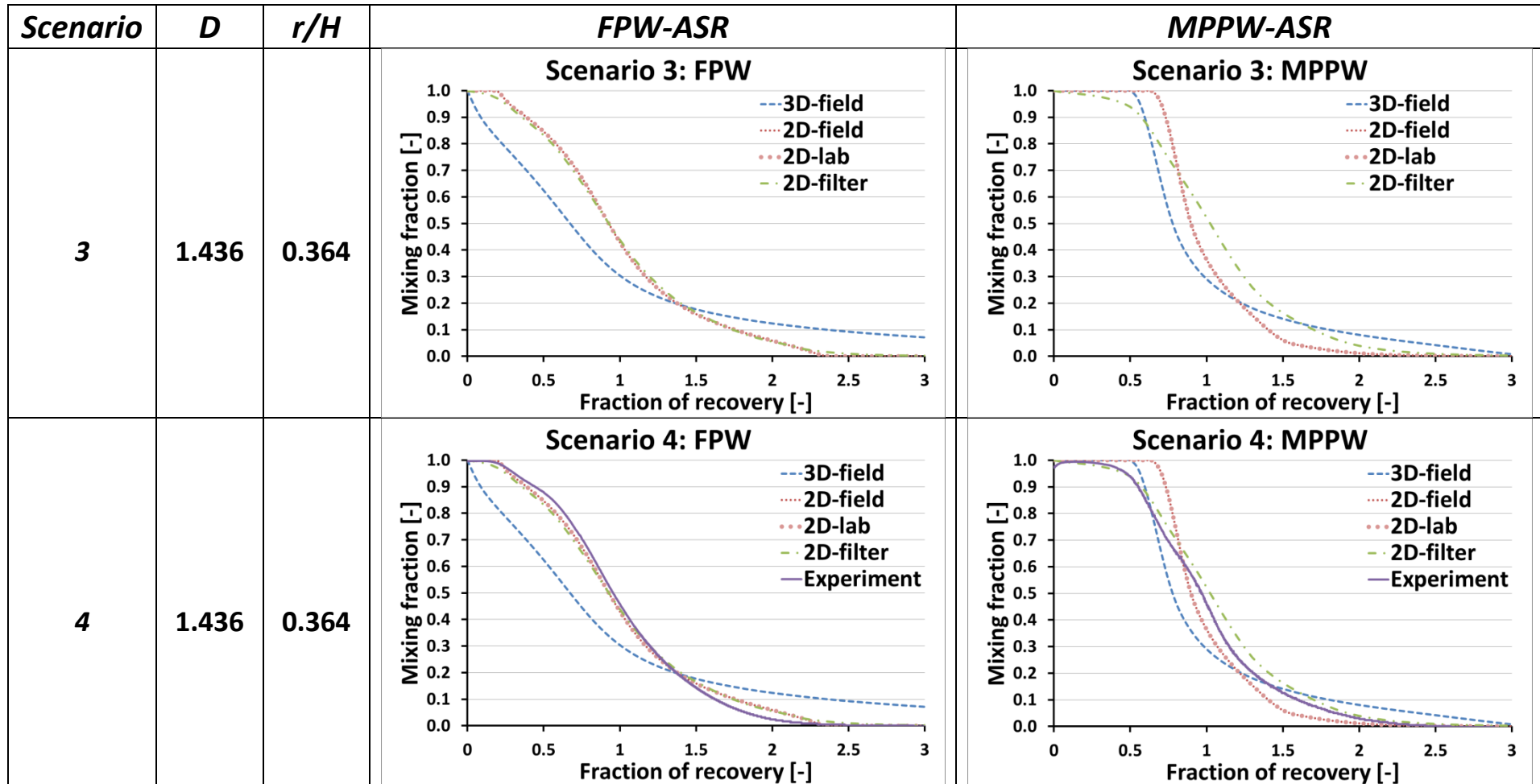


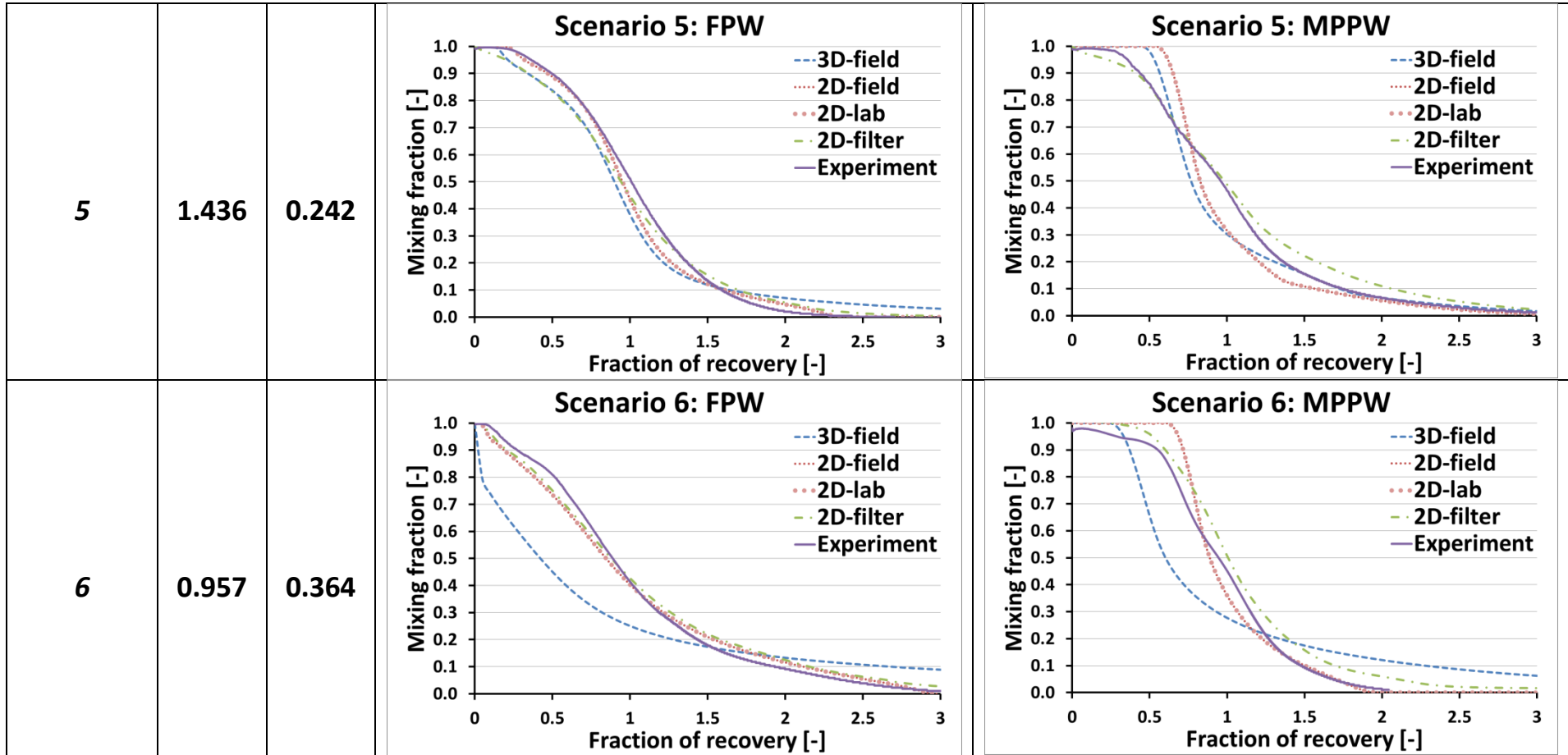
Note that the results of the 2D-field model were equal to those of the 2D-lab model. The thick black line indicates the location of the constant head boundary in the experimental set-up.

7.4. Vertical position of the centre of mass of freshwater ( $z_{cm}$ ) in the representative numerical 3D- and 2D-field settings

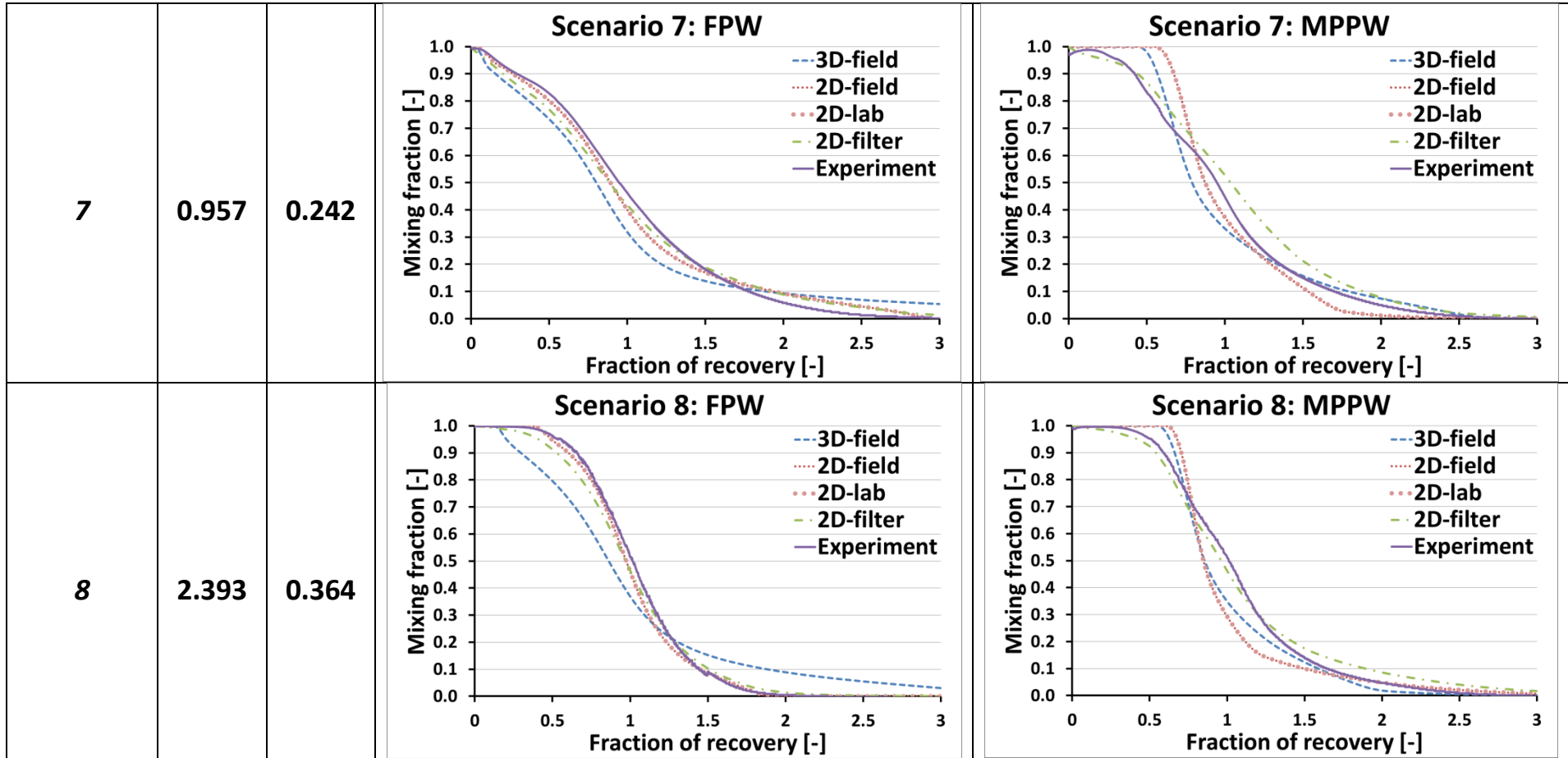
	$r/H = 0.364$		$r/H = 0.242$	
	$z_{cm, 3D}$	$z_{cm, 2D}$	$z_{cm, 3D}$	$z_{cm, 2D}$
$D = 0.957$	18.8	16.3	17.3	16.0
$D = 1.436$	17.9	15.4	16.3	15.4
$D = 2.393$	16.7	14.5	15.2	14.6

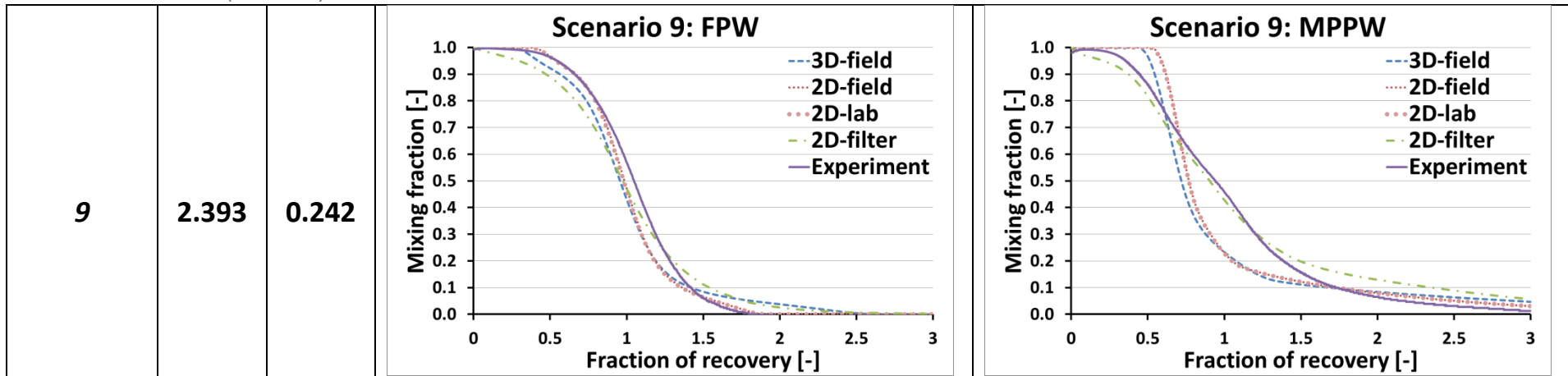
7.5. Mixing fraction versus the fraction of recovery for both FPW-ASR and MPPW-ASR in all models for scenarios 3 – 9











7.6. Infiltration pattern for scenario 2 in the experimental set-up



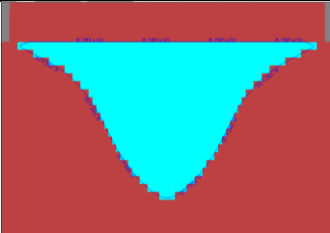
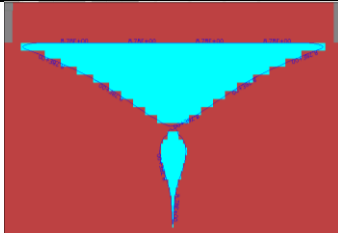
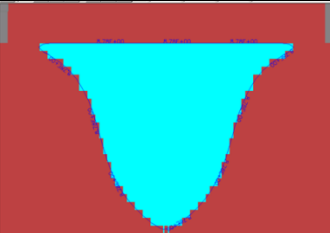
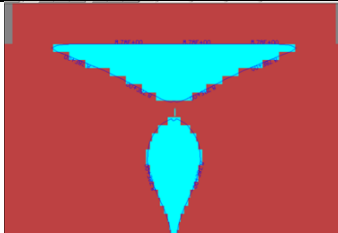
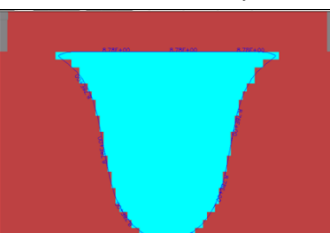

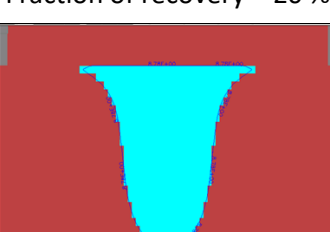
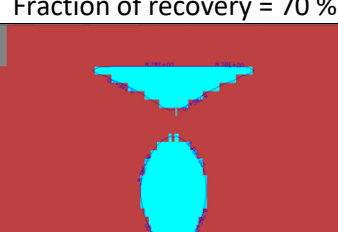
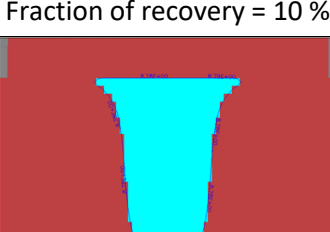
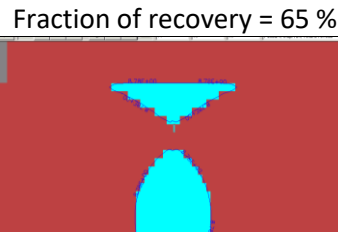
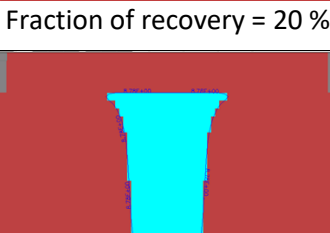
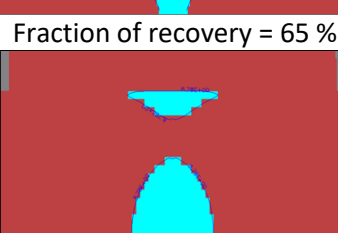
Infiltration\_scenario2.mov (Command Line)

7.7. Evolution of the experimental freshwater body for scenario 4

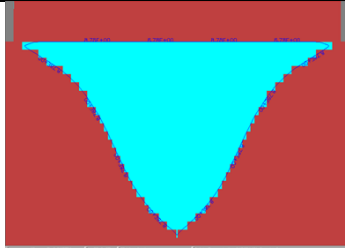
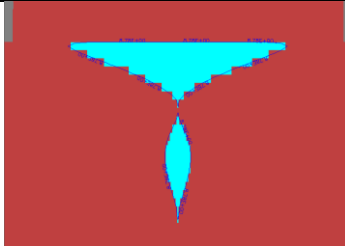
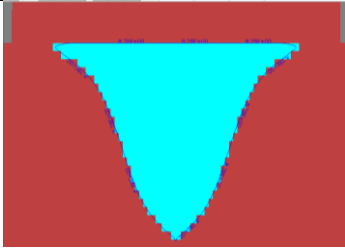
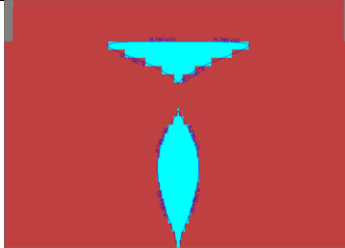
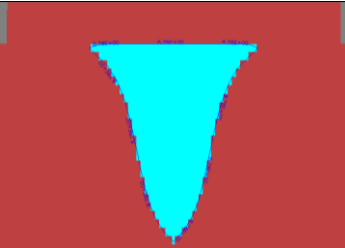
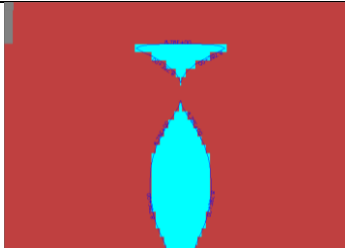
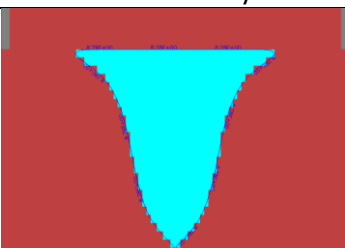
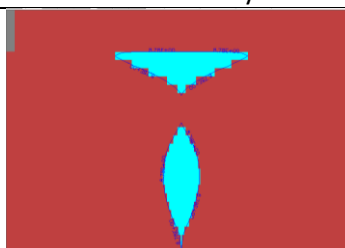
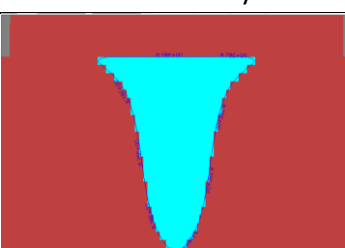
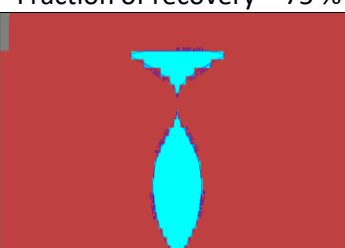

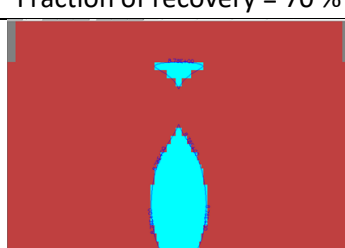


Infiltration\_storage\_recovery\_scenario4.mov (Command Line)

7.8. Freshwater body at the moment of salinization in the 3D-field model

Scenario	D	r/H	FPW-ASR	MPPW-ASR
6	0.957	0.364	 Fraction of recovery = 5 %	 Fraction of recovery = 40 %
4	1.436	0.364	 Fraction of recovery = 5 %	 Fraction of recovery = 65 %
8	2.393	0.364	 Fraction of recovery = 20 %	 Fraction of recovery = 70 %
7	0.957	0.242	 Fraction of recovery = 10 %	 Fraction of recovery = 65 %
5	1.436	0.242	 Fraction of recovery = 20 %	 Fraction of recovery = 65 %
9	2.393	0.242	 Fraction of recovery = 40 %	 Fraction of recovery = 65 %

7.9. Freshwater body at the moment of salinization in the 2D-field model

Scenario	D	r/H	FPW-ASR	MPPW-ASR
6	0.957	0.364	 Fraction of recovery = 10 %	 Fraction of recovery = 75 %
4	1.436	0.364	 Fraction of recovery = 25 %	 Fraction of recovery = 80 %
8	2.393	0.364	 Fraction of recovery = 50 %	 Fraction of recovery = 75 %
7	0.957	0.242	 Fraction of recovery = 10 %	 Fraction of recovery = 75 %
5	1.436	0.242	 Fraction of recovery = 30 %	 Fraction of recovery = 70 %
9	2.393	0.242	 Fraction of recovery = 50 %	 Fraction of recovery = 70 %